American Mineralogist, Volume 107, pages 1681–1696, 2022

The efficiency of copper extraction from magma bodies: Implications for mineralization potential and fluid-silicate melt partitioning of copper

Jin-Sheng Zhou[1], Qiang Wang[1,2,3,*], Derek A. Wyman[4], Zhen-Hua Zhao[5], Le Zhang[1], and Peng-Li He[1]

[1]State Key Laboratory of Isotope Geochemistry, Guangzhou Institute of Geochemistry, Chinese Academy of Sciences, Guangzhou 510640, China
[2]CAS Center for Excellence in Deep Earth Science, Guangzhou, 510640, China
[3]College of Earth and Planetary Sciences, University of Chinese Academy of Sciences, Beijing 100049, China
[4]School of Geosciences, University of Sydney, New South Wales 2006, Australia
[5]Key Laboratory of Mineralogy and Metallogeny, Guangzhou Institute of Geochemistry, Chinese Academy of Sciences, Guangzhou 510640, China

Abstract

Multiple factors may downgrade the mineralization potential of an intermediate-felsic intrusion, such as the commonly invoked inefficient fluid exsolution and lack of ore-forming species (metals and their ligands) in magmas. However, other factors may affect the mineralization potential of a magma body but have poorly understood roles in the formation of magmatic-hydrothermal ore deposits. Here, we present a comparison between two Cu mineralizing plutons and a Cu-poor, Fe mineralizing pluton in the Edong district. Efficient fluid exsolution and extraction occurred during the solidification of all three plutons, as evidenced by extensive skarn alteration around them. The results show that the oxidation state of the three plutons is similar (within a range of ~ΔNNO+0.9 to ΔNNO+2.5). A systematic comparison of the Cu contents of a certain suite of minerals of the three plutons shows that the Cu concentrations of all minerals in the Cu mineralizing plutons are lower than those of the Cu-poor Fe mineralizing pluton. This indicates that the Cu mineralizing plutons underwent more efficient copper extraction. Thus, igneous crystals with anomalously low Cu contents may potentially be used as a tool to identify Cu mineralizing magmatic units in a deposit with multiphase intrusions. We suggest that the inefficient copper extraction from plutons may be ascribed to the lack of reduced S species during fluid exsolution or different evolution paths of Cu and Cl during magma crystallization.

Keywords: Geothermobarometry, fluid exsolution, copper deposit, magma, ore-forming potential

Introduction

Magmatic-hydrothermal ore deposits, including porphyry (Cooke et al. 2005; Seedorff et al. 2005; Sillitoe 2010), skarn (Meinert et al. 2005; Chang et al. 2019), and epithermal type deposits (Hedenquist et al. 1998; Simmons et al. 2005), are the primary source of copper for our society (Arndt et al. 2017). There is a consensus that intermediate-felsic intrusions provide most of the copper, chlorine, and water that are necessary to produce hydrothermal alteration and ore bodies in porphyry copper systems and associated skarns (Hedenquist and Lowenstern 1994; Candela 1997; Meinert et al. 2003; Richards 2003; Williams-Jones and Heinrich 2005; Sillitoe 2010; Audétat and Simon 2012). The formation of porphyry Cu deposits and associated skarns potentially involves multiple processes (Richards 2013; Wilkinson 2013), such as a contribution from oxidized mantle (e.g., Mungall 2002; Wang et al. 2006), pre-enrichment in the lower crust (e.g., Lee et al. 2012; Chiaradia 2014; Hou et al. 2015; Chiaradia and Caricchi 2017; Zheng et al. 2019), sulfide saturation in shallow magma bodies (e.g., Wilkinson 2013), injection of mafic magmas (e.g., Blundy et al. 2015; Yang et al. 2015; Cao et al. 2018), focused fluid flow, and repetitive fluid injections (e.g., Mercer et al. 2015; Li et al. 2017). There is growing evidence supporting the view that magma bodies with typical concentrations of metals (e.g., ~50–100 ppm Cu) may sustain the formation of economic ore deposits (Cline and Bodnar 1991; Chelle-Michou et al. 2017; Zhang and Audétat 2017, 2018), because most metals have high fluid/melt partition coefficients, leading to significant enrichment of them in exsolved fluids (Zajacz et al. 2008; Audétat 2019). On the basis of this hypothesis, if efficient fluid exsolution occurs, many intermediate-felsic intrusions should have the ability to form economic Cu deposits. Nevertheless, many plutons showing efficient fluid exsolution also lack Cu mineralization, indicating that other factors may suppress the mineralization potential of intrusions. Whole-rock analyses may not be sufficient to provide a better understanding of this question because some fraction of the metals and volatiles in an intrusion are commonly lost after solidification. Comparison of melt inclusion compositions from barren and mineralized plutons could provide important insights into this question, but available data sets show that there is no obvious difference in metal concentrations between barren and mineralizing melts (e.g., Audétat 2015; Zhang and Audétat 2017, 2018). It is noteworthy that the studied barren plutons contain abundant miarolitic cavities that represent fluid pockets, implying inefficient extraction of the fluids out of the magma (e.g., Audétat and Pettke 2003; Zhang and Audétat 2018). It is thus difficult to distinguish whether the lack of mineralization is ascribed to inefficient fluid extraction or other factors.

Here, we present a study of minerals (clinopyroxene, feldspar,

* E-mail: wqiang@gig.ac.cn. Orcid 0000-0001-5095-4062

0003-004X/22/0009–1681$05.00/DOI: https://doi.org/10.2138/am-2021-7951

amphibole, titanite, and apatite) from intrusions associated with the Tonglushan Cu-Fe-Au (1.08 Mt Cu, 60 Mt Fe, 70 t Au, and 508 t Ag; Li et al. 2014), Tieshan Fe-Cu (160 Mt Fe and 0.67 Mt Cu; Li et al. 2014), and Jinshandian Fe (200 Mt Fe; Zhu et al. 2015, 2017) skarns in the Edong district (East China), which is one of the most productive Cu-Fe provinces in China. Extensive skarn alteration has been found around all three plutons, indicating that efficient fluid exsolution and extraction occurred during their solidification. A comparison of the three plutons provides an opportunity to identify potential factors that downgrade the Cu-mineralizing potential of an intermediate-felsic intrusion. Our results suggest that the efficiency of copper extraction from magma bodies by fluids plays a critical role in determining Cu mineralization potential.

Geological background

The three studied skarn deposits are located in the Edong district, which is situated on the northern margin of the Yangtze Craton (Fig. 1). Regional tectonic characteristics and magmatism have been described by Zhou et al. (2020a). Magmatic activity in the Edong district began at ~150 Ma and ceased at ~120 Ma when this area was located in an intraplate setting (e.g., Wang et al. 2004; Li et al. 2008; Hou et al. 2013; Pirajno and Zhou 2015; Zhou et al. 2015, 2020a). Extensive hydrothermal alteration and ore deposit formation accompanied the magmatism (Li et al. 2014; Zhou et al. 2020a). There are more than 70 economic Cu-Fe-Au-(Mo-W) deposits within the Edong district, which is a very productive Cu-Fe province (Fig. 1; Li et al. 2014). Skarn and porphyry types are the main alteration-mineralization styles. The skarn deposits sampled for this study, which include the Tonglushan Cu-Fe-Au, Tieshan Fe-Cu, and Jinshandian Fe deposits (Fig. 2), have different metal endowments.

The Tonglushan Cu-Fe-Au skarn deposit is the largest ore deposit in the Edong district and contains 1.08 Mt Cu (~1.8 wt% Cu), 60 Mt Fe (~41 wt% Fe), 70 t Au (~0.38 g/t Au), and 508 t Ag (Li et al. 2014). The Tonglushan deposit contains 12 ore bodies, which are located at the contact zones between the quartz monzodiorite and carbonate rocks or large carbonate xenoliths within the quartz monzodiorite (Fig. 2c). Most ore bodies have lenticular shapes and are 200–500 m in length and 30–110 m in thickness, with vertical extents of 100–500 m (Yu et al. 1985). In addition, ore-bearing breccia pipes have been found at deep levels (Liu et al. 2005). Skarn alteration developed both within the pluton (i.e., endoskarn) and carbonate rocks (i.e., exoskarn) but ore bodies are mainly distributed in exoskarn zones (Zhao et al. 2012). The minerals formed in the prograde stage are andradite, grossular, diopside, hedenbergite, scapolite, and plagioclase, followed by a retrograde alteration assemblage that includes epidote, actinolite, pargasite, phlogopite, chlorite, fluorite, quartz, serpentine, illite, montmorillonite, kaolinite, and dickite (Li et al. 2014; Chen et al. 2019). Ore minerals, including magnetite, hematite, chalcopyrite, bornite, chalcocite, molybdenite, native gold and electrum, are generally associated with retrograde minerals (Li et al. 2014). $^{40}Ar/^{39}Ar$ dating of the phlogopite in the skarn gives an age of ~140 Ma (Li et al. 2014). The quartz monzodiorite pluton has a zircon U-Pb age of 142 ± 1 Ma (Li et al. 2014). Several albitite dikes cut the pluton and skarns (Fig. 2c), indicating that they were intruded after mineralization.

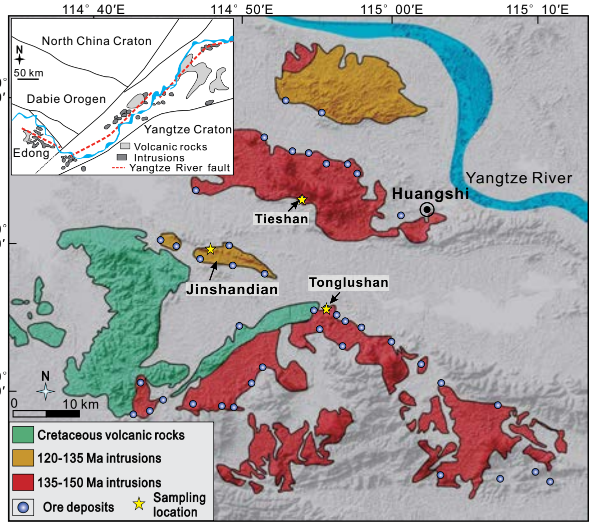

Figure 1. Simplified geological map showing the distribution of Cretaceous intrusions, volcanics and magmatic-hydrothermal ore deposits in the Edong District. Modified from Xie et al. (2011) and Li et al. (2014). The inset map shows regional-scale characteristics and the location of the Edong District (modified from Li et al. 2009). (Color online.)

The Tieshan Fe-Cu skarn deposit contains 160 Mt Fe (~53 wt% Fe) and 0.67 Mt Cu (~0.6 wt% Cu) (Li et al. 2014). Six large orebodies have been found along the contact between the quartz diorite and carbonate rocks (Fig. 2a). Most ore bodies are 480–920 m in length and 10–180 m in thickness, with vertical extents of 200–700 m (Shu et al. 1992). Skarn minerals include garnet, diopside, scapolite, phlogopite, actinolite, albite, plagioclase, epidote, chlorite, tremolite, and pargasite (Li et al. 2014). The phlogopite within the skarns has a $^{40}Ar/^{39}Ar$ age of 142 ± 3 Ma (Xie et al. 2011). The ore minerals are dominated by magnetite, pyrite, chalcopyrite, pyrrhotite, and hematite (Hu et al. 2017). The ore-forming pluton, the quartz diorite, has a zircon U-Pb age of 140.9 ± 1.2 Ma (Xie et al. 2007).

The Jinshandian Fe skarn deposit is situated on the southern and western margins of the Jinshandian pluton (Fig. 2b) and contains 200 Mt Fe (~42.3 wt% Fe) (Zhu et al. 2015, 2017), whereas Cu and Au are absent (Shu et al. 1992). More than 130 ore bodies have been found at the contact zones between the Jinshandian pluton and carbonate or clastic rocks (Fig. 2b), and most of them occur as lenses and veins (Zhu et al. 2015). The skarn mineral assemblages include diopside, phlogopite, scapolite, and amphibole, with minor serpentine, garnet, titanite, and epidote (Zhu et al. 2015). The phlogopite has a $^{40}Ar/^{39}Ar$ age of 127.6 ± 0.9 Ma (Zhu et al. 2017). The ore mineralogy is dominated by magnetite (Shu et al. 1992), which commonly occurs with diopside and phlogopite (Zhu et al. 2017). In addition, anhydrite and pyrite also exist. Anhydrite is present within country rocks, the contact zones between ore body and country rocks, and retrograde skarns in the form of veins or massive aggregates (Zhu et al. 2017). The quartz diorite pluton has zircon U-Pb ages of 127.4 ± 1.2 Ma and 127.6 ± 0.7 Ma (Zhu et al. 2017).

The Tieshan plutonic samples consisting of plagioclase (40–50%), hornblende (10–15%), clinopyroxene (10–15%),

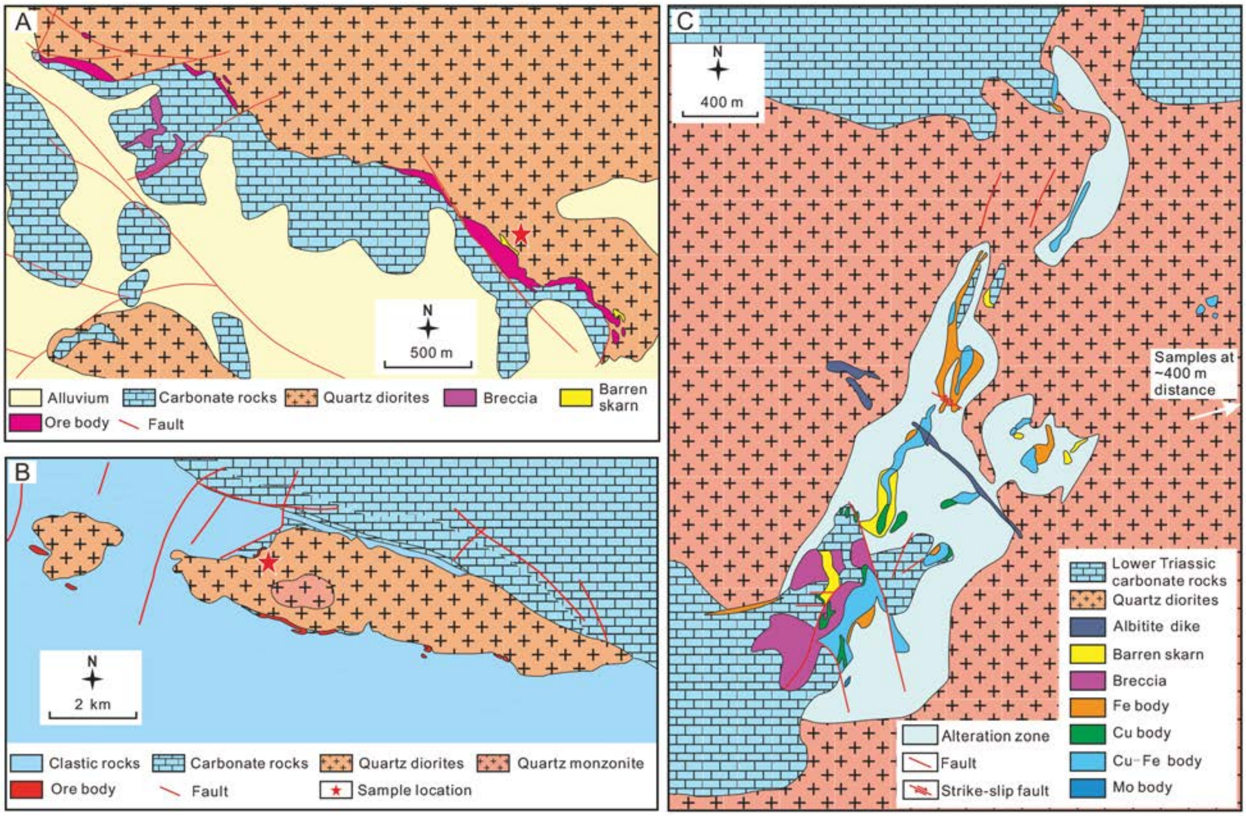

Figure 2. (**a**) Geologic map of the Tieshan Fe-Cu deposit (from Zhu et al. 2019); (**b**) Geologic map of the Jinshandian Fe deposit (modified from Zhu et al. 2017); (**c**) Geologic map of the Tonglushan Fe deposit (from Li et al. 2014). (Color online.)

K-feldspar (5–10%), quartz (5–10%), and minor magnetite, biotite, and titanite, are adjacent to an endoskarn zone (Fig. 2a). The Tonglushan plutonic samples, containing plagioclase (50–60%), K-feldspar (10–20%), quartz (10–20%), hornblende (10–20%) and minor biotite, titanite, and magnetite, were collected from an old mining pit, which is several hundred meters from the current mining location (Fig. 2c). The Jinshandian plutonic rocks consisting of plagioclase (30–40%), K-feldspar (20–30%), hornblende (15–20%), clinopyroxene (5–10%), quartz (5–10%), and minor titanite, biotite, and magnetite, are adjacent to the Jinshandian western ore bodies (Fig. 2b). The plutonic samples of the Tonglushan and Tieshan deposits are the same as those reported in Zhou et al. (2020a). All analyses of Jinshandian deposit samples are new. Minerals with homogeneous interiors or regular zoning patterns that indicate magmatic origin were selected for major and trace element analyses. Some secondary titanite crystals were also analyzed for comparison.

Analytical methods

Whole-rock compositional analysis

Whole-rock major element analyses were performed using X-ray fluorescence spectrometry at Hubei Institute of Geology and Mineral Resource, with analytical errors <2%. Whole-rock trace element analyses were performed using a Perkin-Elmer ELAN 6000 inductively coupled plasma source mass spectrometer (ICP-MS) at the State Key Laboratory of Isotope Geochemistry (SKLaBIG), Guangzhou Institute of Geochemistry, Chinese Academy of Sciences (GIG-CAS). The analytical procedures are similar to Li et al. (2002), with an analytical precision better than 2%.

Mineral compositional analysis

Major element abundances in minerals were analyzed on a JEOL JXA 8100 Superprobe with a 15 kV accelerating voltage, 20 nA beam current, 2 μm probe diameter at the SKLaBIG, GIG-CAS, and a JEOL JXA 8230 electron probe micro-analyzer (EPMA) with a 15 kV accelerating voltage, 20 nA beam current, 1 μm probe diameter, at the Key Laboratory of Mineralogy and Metallogeny of Guangzhou Institute of Geochemistry, GIG-CAS. The EPMA was calibrated using natural and synthetic standards and analytical results were reduced using ZAF (Z: atomic number; A: absorption; F: fluorescence) correction routines.

Mineral trace element analyses were performed using an ELEMENT XR (Thermo-Fisher Scientific) inductively coupled plasma sector field mass spectrometry (ICP-SF-MS) coupled with a 193 nm (ArF) Resonetics RESOlution M-50 laser ablation system (LA) in the SKLaBIG, GIG-CAS. All LA-ICP-SF-MS spots were located to overlap a conjugate EMPA spot. The spot size was 33 μm, at a pulse energy of ~4 J cm^{-2} and a laser repetition rate of 5 Hz. A smoothing device (The Squid, Laurin Technic) was used to smooth the sample signal. For each spot, counting times were 20 s for gas blank collection (laser off) and 30 s for sample signal detection (laser on). The standards, BCR-2G, BHVO-2G, and GSD-1G, were analyzed for the construction of the calibration line. Trace element concentrations were normalized to that of SiO_2, as determined by EPMA. The TB-1G (USGS reference glass) was analyzed as an unknown sample, and the results are shown in Online Materials[1] Table A7. For apatite, NIST SRM 610 and 612 were analyzed for the calibration and unknown, respectively, and CaO was used as the internal standard. More detailed experimental procedures and data reduction strategies have been described by Zhang et al. (2019).

High-resolution X-ray element mapping

High-resolution X-ray element mapping was employed to image the zoning patterns of titanite, using a Cameca SXFiveFE electron microprobe at the SKLaBIG, GIG-CAS. The operating conditions were 20 kV accelerating voltage and 80 nA beam current.

Table 1. Representative whole-rock major and trace element compositions of the Tonglushan, Tieshan, and Jinshandian plutonic rocks

Deposit	Tonglushan[a] Cu-Fe-Au skarn deposit		Tieshan Fe-Cu skarn deposit[b]						Jinshandian Fe skarn deposit[c]				
Lithology	Quartz monzodiorite		Quartz diorite						Quartz diorite				
Sample	HB-008	HB-009	HB001	HB003	HB006	HB007	ts1	ts4	Jsd-1	Jsd-2	Jsd-3	Jsd-6	Jsd-8
						Major oxides(wt%)							
SiO_2	63.68	62.64	63.77	64.73	64.19	62.84	63.12	62.82	68.24	66.57	58.08	66.38	69.65
TiO_2	0.55	0.56	0.54	0.57	0.50	0.56	0.67	0.65	0.65	0.69	0.86	0.85	0.50
Al_2O_3	15.92	16.17	15.81	15.76	15.98	16.47	16.15	16.18	15.11	15.50	14.59	15.77	14.34
TFe_2O_3	4.89	4.86	4.30	4.32	4.28	4.18	4.83	4.82	1.71	1.91	9.78	1.89	3.15
MnO	0.08	0.09	0.05	0.06	0.07	0.05	0.07	0.07	0.02	0.03	0.04	0.03	0.04
MgO	1.44	0.86	1.62	1.68	1.42	1.88	1.81	1.88	1.11	1.05	1.35	1.10	0.90
CaO	4.98	5.55	3.99	3.68	4.21	3.94	4.20	4.29	2.43	2.95	3.67	3.29	1.02
Na_2O	4.35	4.53	4.84	5.02	5.57	5.60	5.07	5.07	6.86	7.44	4.13	7.61	4.44
K_2O	2.75	2.71	3.30	2.97	2.67	3.06	2.98	3.17	1.64	1.21	2.87	1.41	4.91
P_2O_5	0.26	0.26	0.24	0.24	0.23	0.29	0.29	0.29	0.15	0.16	0.20	0.23	0.14
LOI	1.06	1.73	1.32	0.83	0.73	0.75	0.67	0.59	2.00	2.44	4.91	1.34	0.84
Total	99.73	99.73	99.53	99.65	99.63	99.43	99.62	99.60	99.92	99.95	100.48	99.90	99.93
						Trace elements (ppm)							
Cr	6.98	6.65	25.7	25.2	12.9	22.7	19.1	19.2	2.80	2.95	1.60	1.89	2.92
Ni	5.83	6.52	14.46	15.74	8.01	18.5	14.0	14.9	2.34	1.82	2.17	1.52	2.04
Co	9.45	9.29	7.93	10.5	8.75	10.5	10.5	10.6	2.49	2.03	5.15	3.43	2.42
Sc	6.35	5.38	4.98	5.95	5.62	6.29	6.70	6.42	5.38	6.01	6.10	5.17	4.26
V	70.9	68.6	69.0	63.4	60.1	70.6	69.7	71.0	26.8	26.6	43.9	48.2	32.5
Pb	8.78	8.53	23.62	11.22	10.75	8.85	9.19	9.62	3.51	2.61	2.22	4.18	6.12
Rb	93.1	89.3	85.0	72.6	57.3	53.8	95.2	63.9	33.4	25.9	75.4	32.4	182
Cs	1.06	1.11	1.81	1.27	0.56	0.35	0.99	0.57	0.27	0.11	0.93	0.49	0.65
Ba	734	692	1016	985	1210	2238	1157	1245	671	544	815	775	879
Sr	961	983	1609	1433	1786	2100	1467	1531	277	180	190	207	266
Ga	22.3	21.2	24.1	24.5	24.0	23.6	23.9	24.2	19.5	20.0	18.2	20.2	17.8
Ta	1.03	1.08	0.75	0.78	0.80	0.72	0.86	0.82	2.26	2.10	1.95	2.28	2.16
Nb	18.1	18.0	13.4	14.2	15.0	13.8	14.3	14.0	29.5	28.4	30.1	34.5	22.3
Hf	4.04	4.19	5.07	5.28	3.56	2.73	5.23	5.17	8.45	10.67	7.41	9.47	6.34
Zr	131	131	166	168	121	79	187	184	305	415	273	367	227
Y	17.0	18.3	13.3	13.8	15.0	14.3	16.3	15.9	29.7	30.4	21.4	36.2	20.4
Th	13.4	13.1	7.5	8.3	6.4	7.7	10.1	9.9	21.0	19.3	15.2	18.6	23.5
U	3.24	2.94	2.24	2.35	1.73	1.44	2.24	2.21	3.23	3.12	2.39	3.13	5.52
La	51.0	51.0	42.6	46.6	53.4	58.7	59.6	61.7	43.5	49.5	75.4	64.1	35.4
Ce	97.7	96.5	84.8	90.1	105	118	113	116	93.9	103	126	136	69.5
Pr	10.3	10.0	9.32	9.82	11.4	13.0	13.3	13.6	11.1	11.8	13.3	16.2	7.95
Nd	37.8	38.2	35.4	36.6	42.2	50.4	50.0	51.3	39.6	41.1	44.9	57.1	28.0
Sm	6.83	6.94	6.41	6.91	7.76	8.33	7.64	7.67	6.69	6.71	6.59	8.99	4.55
Eu	1.78	1.78	1.73	1.71	1.91	2.16	1.90	1.92	1.38	1.32	1.20	1.87	0.85
Gd	4.93	5.03	4.40	4.50	5.08	5.59	4.39	4.37	5.35	5.16	4.21	6.57	3.37
Tb	0.63	0.62	0.55	0.58	0.66	0.64	0.64	0.61	0.91	0.91	0.74	1.15	0.59
Dy	3.34	3.43	2.85	2.86	3.12	2.94	3.36	3.31	5.36	5.52	4.07	6.80	3.61
Ho	0.63	0.69	0.49	0.49	0.56	0.54	0.60	0.58	1.08	1.11	0.77	1.33	0.73
Er	1.88	2.07	1.29	1.46	1.50	1.47	1.61	1.56	3.11	3.23	2.06	3.78	2.16
Tm	0.25	0.28	0.18	0.18	0.22	0.20	0.22	0.22	0.49	0.50	0.29	0.59	0.34
Yb	1.71	1.66	1.09	1.20	1.20	1.23	1.40	1.41	3.26	3.42	1.86	3.76	2.31
Lu	0.24	0.24	0.15	0.16	0.21	0.15	0.23	0.22	0.53	0.56	0.30	0.60	0.38
Sr/Y	56.4	53.8	121	104	119	147	90.1	96.5	9.33	5.92	8.88	5.73	13.1
Eu/Eu*	0.94	0.92	0.99	0.94	0.93	0.97	1.00	1.01	0.70	0.68	0.69	0.75	0.66
Dy/Dy*	0.52	0.54	0.64	0.59	0.61	0.55	0.57	0.56	0.56	0.54	0.53	0.57	0.51
$(La/Yb)_N$	21.1	21.7	27.6	27.6	31.6	33.9	30.2	31.1	9.47	10.3	28.7	12.1	10.8[c]

Note: LOI = loss on ignition.
[a] Data source: Zhou et al. (2020a).
[b] Data source: Zhou et al. (2020a).
[c] Data source: This study.

Results

All of the whole-rock and mineral data used in this study can be found in Online Materials[1] Tables A1 to A6, including data previously published in Zhou et al. (2020a). Representative whole-rock and mineral data are shown in Tables 1–6. The majority of mineral major and trace element analyses both in this study and Zhou et al. (2020a) were performed at the SKLaBIG, GIG-CAS.

Whole-rock compositions

The representative whole-rock chemical compositions of the Tonglushan, Tieshan, and Jinshandian plutonic rocks are in Table 1, and the full list of analyses is provided in Online Materials[1] Table A1. The Tonglushan plutonic rocks have SiO_2 = 62.6–63.7 wt%, MgO = 0.86–1.44 wt%, Na_2O = 4.35–4.53 wt%, K_2O = 2.71–2.75 wt%, and Mg# = 26.0–36.9. For trace elements of interest, concentrations or ratios are, respectively: Zr = 131 ppm; Sr = 961–983 ppm; Y = 17.0–18.3 ppm; Eu/Eu* = 0.92–0.94 ppm; Dy/Dy*, defined as $Dy/(Dy^*) = Dy_N/[La_N^{(4/13)} * Yb_N^{(9/13)}]$ (Davidson et al. 2013) = 0.52–0.54; $(La/Yb)_N$ = 21.1–21.7. The Tieshan intrusion rocks have SiO_2 = 62.4–64.7 wt%, MgO = 1.42–1.92 wt%, Na_2O = 4.84–5.60 wt%, K_2O = 2.67–3.30 wt%, and Mg# = 39.7–47.1. Trace element concentrations or ratios include: Zr = 79–200 ppm; Sr = 1337–2310 ppm; Y = 13.3–16.8 ppm; Eu/Eu* = 0.88–1.02 ppm; Dy/Dy* = 0.55–0.64; $(La/Yb)_N$ = 23.1–33.9. The Jinshandian quartz diorites

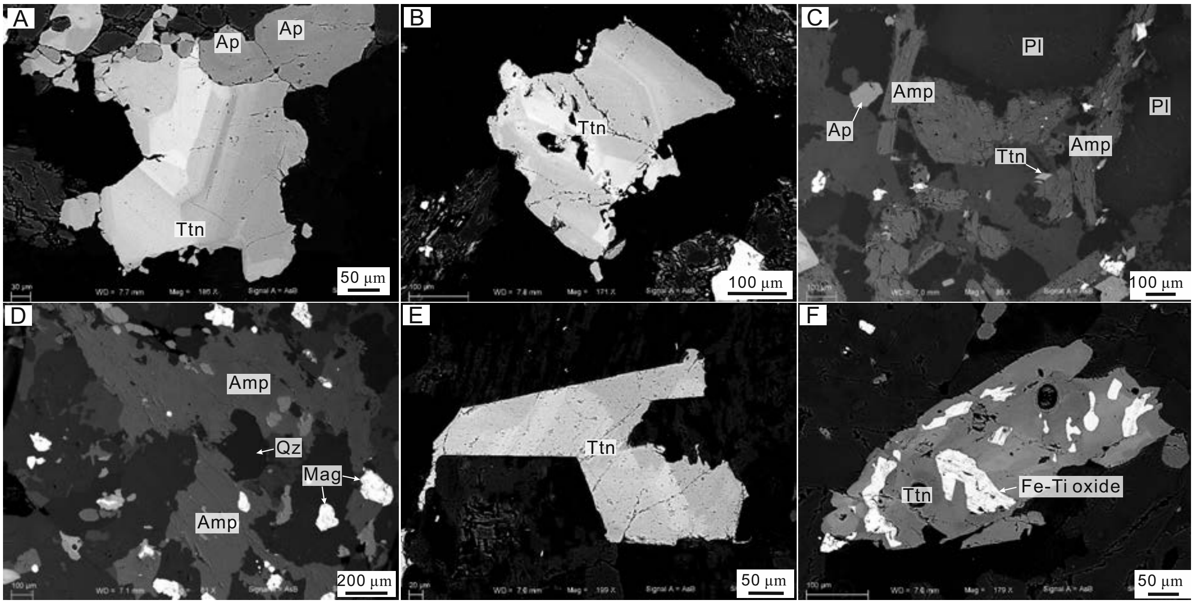

FIGURE 3. Photographs of titanites from the three plutons. (**a**) Magmatic titanite and apatite grains in the Tonglushan pluton; (**b**) magmatic titanite in the Tonglushan pluton; (**c**) euhedral amphibole in the Tieshan pluton; (**d**) anhedral amphibole in the Tieshan pluton; (**e**) magmatic titanite in the Jinshandian pluton; (**f**) secondary titanite with Fe-Ti oxide inclusions with irregular shapes in the Jinshandian pluton. Mineral abbreviations: Ttn = titanite; Ap = apatite; Amp = amphibole; Pl = plagioclase; Qz = quartz; Mag = magnetite.

have SiO_2 = 58.1–71.0 wt%, MgO = 0.40–1.71 wt%, Na_2O = 2.53–9.70 wt%, K_2O = 0.18–4.91 wt%, and Mg# = 21.5–59.6. Trace elements concentrations or ratios include: Zr = 98.2–415 ppm; Sr = 129–392 ppm; Y = 14.0–36.2 ppm; Eu/Eu* = 0.50–1.03 ppm; Dy/Dy* = 0.47–0.60; $(La/Yb)_N$ = 8.3–28.7.

Mineral major and trace element compositions

Clinopyroxene. Clinopyroxene is present in the Tieshan and Jinshandian plutons, but no clinopyroxene crystal was found in the Tonglushan samples. Most of the Tieshan clinopyroxene crystals are small in size (100–500 μm in length), and most of them are euhedral. Compositionally, they are diopside and in the range of $Wo_{47–49}En_{36–38}Fs_{14–17}$, with Mg# [Mg/(Mg+$Fe_{total}$)] of 70–74 (Zhou et al. 2020a). For certain trace elements of interest, concentrations are Cu = 0.02–0.94 ppm; Mo = 0.01–0.74 ppm; Zn = 166–210 ppm; Pb = 0.50–7.26 ppm; Sr = 19.7–58.3 ppm. The Jinshandian clinopyroxene crystals are 100–800 μm in length with a euhedral morphology, and most are diopside with compositions of $Wo_{49–53}En_{36–42}Fs_{8–14}$ and Mg# of 69–76. They have Cu = 0.65–0.93 ppm, Zn = 132–179 ppm, Pb = 0.61–1.96 ppm, and Sr = 34.6–85.4 ppm.

Feldspar. Feldspar group minerals are the most common phase in the three plutons. Most Tonglushan and Tieshan plagioclase show normal zoning or oscillatory zoning, and the cores are in equilibrium with their whole-rock compositions (Zhou et al. 2020a). Setting aside the compositional zoning, the plagioclase An values of the Tonglushan, Tieshan, and Jinshandian plutons are $An_{20–58}$, $An_{10–44}$, and $An_{14–30}$. Concentrations of certain trace elements for the Tonglushan, Tieshan, and Jinshandian plagioclase are: Cu = 0.06–1.31, 0.03–1.80, and 10.5–12.1 ppm; Zn = 3.16–46.8, 0.56–44.1, and 2.68–5.48 ppm; Pb = 2.90–9.30, 1.04–35.2, and 2.82–12.8 ppm; Sr = 1088–2752, 1396–4927, and 1605–2962 ppm. A small number of analyses show that the Tieshan and Jinshandian K-feldspar crystals have Cu of 0.04–1.80 and 1.81–13.0 ppm, respectively.

Amphibole. Amphibole is present in all three plutons. Most amphibole crystals in the Tonglushan pluton are euhedral, with sizes ranging from 0.2 to 1.6 mm in length. Some amphibole crystals contain titanite and apatite inclusions. Compositionally, the Tonglushan amphibole crystals have Mg# of 62–72, Cu = 0.08–1.15 ppm, Mo = 0.06–1.14 ppm, Zn = 125–220 ppm, Sr = 9.17–32.9 ppm. Two amphibole populations (euhedral vs. anhedral grains) may be recognized in the Tieshan pluton (Figs. 3c and 3d). Some amphibole has a close spatial relationship with clinopyroxene, and they are in contact. Compositions for the euhedral and anhedral amphibole crystals are Mg# = 62–73 and 60–69; Cu = 0.1–2.06 and 0.03–1.01 ppm; Mo = 0.01–2.07 and 0.01–0.55 ppm; Zn = 65.7–380 and 276–395 ppm; Sr = 26.4–294 and 18.1–73.6 ppm. Similarly, euhedral and anhedral amphibole populations may be identified in the Jinshandian pluton. Euhedral and anhedral amphibole crystals occur in different hand samples and have Mg# = 57–85 and 57–73, Cu = 3.32–5.28 and 1.39–2.35 ppm, Zn = 152–225 and 260–292 ppm, and Sr = 7.92–51.5 and 15.1–62.4 ppm, respectively.

Titanite. Titanite is present in the host plutons of all three deposits (Fig. 3). Titanite grains in the Tieshan pluton are interstitial, but the small sizes make microanalysis difficult (Fig. 3c). Analyzed titanite crystals in this study are from the Tonglushan and Jinshandian plutons. On the basis of a combination of backscattered electron images and crystal morphologies, titanite crystals may be divided into magmatic and secondary crystals. One population of titanite commonly exhibits oscillatory zoning (Figs. 3a and 3b), sector zoning, or superimposed oscillatory zoning on sector zoning (Fig. 3b), which are interpreted as magmatic textures (Paterson and Stephens 1992). A second population of titanite shows no regular zoning patterns and commonly contains Fe-Ti oxide inclusions with irregular shapes (Fig. 3f); this population is interpreted as secondary. Compositionally, the titanite crystals from the Tonglushan pluton have Cu = 1.83–3.61 ppm, Mo = 38.9–134 ppm, Zn = 4.68–24.4 ppm, Sr = 2.35–53.6 ppm, Cr = 6.81–19.9 ppm, and Zr = 325–3929 ppm. In the Jinshandian pluton, the magmatic titanite crystals contain Cu = 5.59–6.69 ppm, Zn = 11.0–13.3 ppm, Sr = 44.0–72.0 ppm, Cr = 5.55–15.8 ppm, and Zr = 849–7209 ppm, and the secondary titanite crystals have Cu = 5.78–6.66 ppm, Zn = 12.0–13.5 ppm, Sr = 71.2–147 ppm, Cr = 87.0–303 ppm, and Zr = 760–2780 ppm. It is noteworthy that magmatic titanite crystals show sector zoning because this feature exerts important controls on trace element concentrations (Paterson and Stephens 1992).

Apatite. Apatite is a minor but ubiquitous phase in the Tonglushan, Tieshan, and Jinshandian plutons. Apatite inclusions commonly occur in other minerals, but most grains in the Tonglushan pluton are bigger than those in the other two plutons (Fig. 3a). The larger sizes (up to 200 μm in length) make microbeam analysis of the Tonglushan apatite crystals feasible. Most Tonglushan apatite crystals are fluorapatite, with F = 2.85–3.69 wt%. They have Cu = 0.03–0.70 ppm, Zn = 0.09–3.19 ppm, Sr = 427–517 ppm, La = 1726–3959 ppm, and Y = 148–403 ppm.

TABLE 2. Representative clinopyroxene major and trace element compositions

Pluton	Tieshan[a]							Jinshandian[b]						
Sample	TS-1							Jsd-2						
Spot	100	101	103	104	107	118	119	38	40	41	45	49	54	55
							Oxide contents (wt%)							
SiO_2	54.00	53.48	53.58	53.76	53.53	53.61	53.99	53.24	52.43	52.60	52.77	52.06	52.91	52.35
TiO_2	0.14	0.16	0.06	0.09	0.10	0.14	0.11	0.20	0.11	0.09	0.13	0.39	0.22	0.27
Al_2O_3	0.63	0.55	0.48	0.47	0.49	0.58	0.45	0.76	0.90	0.61	0.57	1.40	0.75	0.75
FeO	8.40	8.51	8.68	8.64	8.72	8.81	8.59	8.49	8.25	8.35	8.32	8.80	8.04	8.26
MnO	0.57	0.54	0.60	0.66	0.55	0.60	0.63	0.29	0.23	0.27	0.29	0.23	0.33	0.31
MgO	13.07	13.17	12.73	12.73	12.71	12.50	12.93	13.16	13.36	13.11	14.07	12.82	13.35	13.38
CaO	22.72	22.72	22.55	22.68	22.88	23.16	22.80	24.09	24.17	24.75	23.21	23.82	24.02	24.33
Na_2O	0.43	0.39	0.54	0.60	0.50	0.55	0.54	0.46	0.61	0.52	0.54	0.72	0.63	0.55
K_2O	b.d.l.	b.d.l.	b.d.l.	b.d.l.	b.d.l.	0.01	0.00	0.01	b.d.l.	b.d.l.	0.01	0.01	0.02	0.01
P_2O_5	0.00	0.00	0.04	0.02	0.06	0.03	0.01	0.01	0.02	0.03	0.03	0.00	0.06	0.02
Cr_2O_3	0.00	0.01	b.d.l.	0.04	0.00	b.d.l.	0.04	b.d.l.	0.01	0.02	0.05	b.d.l.	0.03	b.d.l.
F	b.d.l.	b.d.l.	b.d.l.	b.d.l.	b.d.l.	b.d.l.	b.d.l.	b.d.l.	b.d.l.	b.d.l.	b.d.l.	b.d.l.	b.d.l.	b.d.l.
Cl	0.01	0.01	0.02	b.d.l.	0.00	0.00	b.d.l.	0.01	0.00	b.d.l.	0.01	0.00	b.d.l.	b.d.l.
Total	99.96	99.53	99.26	99.70	99.54	99.98	100.08	100.71	100.08	100.34	100.00	100.24	100.34	100.24
							Trace element contents (ppm)							
Cu	0.53	0.07	0.65	0.02	0.10	0.48	0.51	0.77	0.76	0.65	0.74	0.85	0.93	0.72
Zn	166	171	210	167	172	166	175	145	132	142	172	144	167	152
Pb	0.73	0.63	3.41	0.66	0.64	0.60	1.78	0.98	1.46	0.61	1.96	0.62	0.94	0.79
P	12.6	6.27	9.24	5.65	18.71	10.9	10.7	11.3	6.56	10.2	8.09	11.4	10.9	10.4
Li	53.0	55.3	57.7	55.4	62.6	64.5	62.1	57.9	49.1	48.0	65.8	59.2	64.4	50.6
Sc	101	87.4	90.9	108.0	88.5	92.9	96.6	78.1	72.5	81.4	47.7	87.5	77.8	65.8
V	95.6	98.7	131	93.2	130	94.6	116	150	152	156	116	183	203	140
Cr	12.9	16.1	31.6	26.9	38.8	15.4	24.4	62.9	51.1	68.4	54.6	81.4	338	113
Co	38.2	42.8	42.0	44.2	42.3	42.3	40.3	35.7	35.2	35.3	43.3	38.8	37.4	35.2
Ni	23.8	28.4	25.5	30.2	23.5	30.0	21.6	55.0	44.7	46.9	63.4	48.7	96.5	65.8
Ga	7.38	8.18	12.3	7.12	10.4	7.64	8.85	13.3	11.1	8.79	15.2	15.5	20.1	12.7
Rb	0.00	0.03	1.28	0.03	0.00	0.05	0.81	0.00	0.04	0.01	0.17	0.02	0.00	0.00
Sr	54.1	37.9	32.7	23.6	37.7	27.2	41.0	85.4	76.7	52.9	34.6	64.0	69.9	74.6
Y	12.1	7.98	23.6	6.74	15.2	7.14	14.5	20.1	17.5	12.4	52.2	26.5	25.3	23.6
Zr	22.4	24.0	87.7	21.1	78.9	13.3	41.1	103	51.2	76.6	23.6	87.8	214	108
Nb	0.04	0.02	0.20	0.02	0.06	0.01	0.06	0.07	0.05	0.01	0.03	0.10	0.22	0.06
Cs	0.00	0.00	0.29	0.00	0.00	0.03	0.20	0.01	0.00	0.00	0.02	0.00	0.00	0.00
Ba	0.05	0.00	1.46	0.00	0.00	0.00	0.63	0.15	0.23	0.22	0.41	0.10	0.02	0.00
La	14.0	11.8	33.5	9.9	22.3	10.7	16.5	22.9	17.7	10.5	23.0	24.6	37.8	23.8
Ce	44.2	33.6	94.6	26.1	62.7	27.1	50.1	71.7	57.4	33.0	82.8	80.7	112.2	75.4
Pr	6.25	4.31	12.7	3.14	8.85	3.39	7.27	10.5	8.39	5.00	13.4	12.3	14.7	11.0
Nd	29.8	17.9	53.5	15.6	36.4	14.5	32.8	45.7	37.3	21.0	65.9	55.7	58.9	47.0
Sm	5.11	3.58	10.07	3.08	6.32	2.74	6.20	9.16	7.69	4.68	16.42	11.81	9.39	9.48
Eu	1.25	0.66	1.94	0.58	1.43	0.54	1.37	2.33	1.77	1.08	2.79	2.49	2.04	1.87
Gd	3.64	2.63	7.59	1.72	4.86	2.28	4.62	7.03	6.06	3.83	14.08	9.68	7.73	7.94
Tb	0.48	0.31	0.79	0.20	0.56	0.25	0.58	0.89	0.72	0.51	1.99	1.11	0.89	0.93
Dy	2.55	1.62	4.57	1.32	2.84	1.41	3.12	4.14	3.41	2.79	10.84	6.02	4.93	4.79
Ho	0.37	0.27	0.85	0.20	0.57	0.25	0.50	0.64	0.57	0.40	1.87	0.93	0.78	0.81
Er	1.32	0.75	2.39	0.61	1.25	0.82	1.63	1.72	1.64	1.22	4.94	2.69	2.28	2.07
Tm	0.18	0.12	0.31	0.09	0.18	0.10	0.16	0.24	0.23	0.20	0.64	0.28	0.26	0.23
Yb	1.30	0.99	2.01	0.67	1.20	0.66	1.51	1.39	1.37	1.35	4.18	1.86	2.65	1.70
Lu	0.27	0.17	0.38	0.19	0.30	0.17	0.24	0.28	0.25	0.23	0.65	0.30	0.43	0.36
Hf	1.51	1.62	5.48	1.27	4.81	0.95	3.00	3.70	2.73	3.21	2.26	5.32	6.54	3.68
Ta	0.00	0.00	0.01	0.00	0.01	0.00	0.00	0.08	0.01	0.01	0.00	0.01	0.03	0.00
Th	0.04	0.06	0.51	0.12	0.14	0.23	0.27	0.04	0.04	0.04	0.18	0.11	0.13	0.04
U	0.01	0.01	0.34	0.03	0.04	0.02	0.07	0.01	0.00	0.01	0.02	0.02	0.01	0.01

Note: b.d.l. = below detection limit.
[a] Data source: Zhou et al. (2020a).
[b] Data source: This study.

Table 3. Representative feldspar major and trace element compositions

Pluton	Tonglushan[a]					Tieshan[a]						Jinshandian[b]				
Sample	HB008					TS-1	TS-3	HB002	HB004	HB007	HB001	Jsd-2				
Spot	24	43	45	46	47	110	206	237	88	163	211	71	72	82	83	89
							Oxide contents (wt%)									
SiO_2	61.87	53.56	53.56	54.71	55.89	65.44	62.00	63.32	62.67	65.13	62.25	65.11	64.92	62.20	63.62	63.90
TiO_2	b.d.l.	b.d.l.	b.d.l.	b.d.l.	b.d.l.	b.d.l.	0.05	b.d.l.	0.03	b.d.l.	b.d.l.	0.03	0.01	b.d.l.	b.d.l.	0.02
Al_2O_3	23.59	28.58	27.47	27.80	27.41	22.56	22.74	23.23	23.03	21.23	23.06	21.42	21.21	23.18	22.49	21.45
FeO	0.24	0.17	0.16	0.24	0.26	0.13	0.14	0.10	0.16	0.20	0.14	0.20	0.21	0.16	0.13	0.13
MnO	0.01	b.d.l.	b.d.l.	0.03	b.d.l.	b.d.l.	0.03	b.d.l.	0.01	0.04	0.02	b.d.l.	0.01	b.d.l.	b.d.l.	b.d.l.
MgO	0.01	0.01	0.03	0.02	b.d.l.	b.d.l.	b.d.l.	b.d.l.	0.01	b.d.l.	b.d.l.	b.d.l.	b.d.l.	b.d.l.	b.d.l.	0.00
CaO	5.83	11.93	11.52	11.38	10.51	3.75	4.37	5.06	4.98	3.22	4.74	3.75	3.00	5.17	4.92	4.22
Na_2O	7.93	4.99	5.04	5.47	5.34	7.42	9.32	8.49	8.47	9.48	8.72	9.55	10.07	8.86	9.22	8.18
K_2O	0.53	0.15	0.18	0.17	0.19	0.26	0.32	0.30	0.37	0.85	0.34	0.36	0.33	0.29	0.22	0.32
P_2O_5	0.01	0.03	0.01	0.01	0.01	0.02	0.02	b.d.l.	0.02	b.d.l.	0.01	b.d.l.	0.03	0.00	0.03	b.d.l.
Cr_2O_3	b.d.l.	0.04	0.26	0.35	b.d.l.	b.d.l.	b.d.l.	0.03	0.31	0.00	0.14	b.d.l.	b.d.l.	b.d.l.	b.d.l.	0.20
F	b.d.l.	b.d.l.	b.d.l.	b.d.l.	b.d.l.	b.d.l.	b.d.l.	b.d.l.	b.d.l.	b.d.l.	b.d.l.	b.d.l.	b.d.l.	b.d.l.	b.d.l.	b.d.l.
Cl	b.d.l.	0.01	b.d.l.	0.00	0.01	0.01	0.00	b.d.l.	0.01	b.d.l.	0.01	b.d.l.	b.d.l.	b.d.l.	b.d.l.	b.d.l.
Total	100.01	99.45	98.24	100.17	99.62	99.59	98.98	100.53	100.05	100.15	99.42	100.43	99.78	99.87	100.63	98.41
							Trace element contents (ppm)									
Cu	0.06	0.29	0.71	0.68	0.40	1.21	0.65	0.76	0.87	0.41	0.38	11.69	11.71	11.44	11.69	11.45
Zn	7.47	30.42	6.08	7.21	4.72	3.39	1.27	7.83	6.49	10.1	28.3	2.72	3.16	3.57	3.01	3.44
Pb	9.30	4.89	2.90	5.45	5.53	8.78	6.94	7.60	9.44	9.06	12.49	8.34	9.40	9.32	8.91	9.78
P	44.2	21.4	19.1	27.9	21.7	3.5	24.8	27.9	12.6	34.1	19.4	14.7	20.3	19.7	9.9	16.7
Li	7.26	5.04	0.63	0.91	0.87	2.77	0.00	12.67	7.92	13.06	25.47	2.49	4.31	0.00	1.17	0.34
Sc	2.93	2.14	2.13	2.40	1.71	2.61	2.62	3.20	3.39	2.10	3.07	6.12	5.24	5.24	5.20	5.01
V	0.20	3.28	0.00	0.04	0.12	0.00	0.00	0.37	0.18	0.02	2.63	0.02	0.11	0.23	0.00	0.04
Cr	17.5	31.2	7.4	10.6	12.4	18.0	7.8	10.1	8.6	4.5	6.9	13.1	9.4	14.7	21.0	18.8
Co	0.30	1.91	0.22	0.51	0.14	0.13	0.00	0.06	0.07	0.08	0.58	0.10	0.06	0.02	0.07	0.01
Ni	3.80	0.00	0.00	0.74	0.00	0.00	0.00	0.00	0.00	0.00	0.00	0.79	1.14	0.67	1.21	0.87
Ga	27.6	22.4	20.4	24.3	21.6	29.9	32.6	25.9	26.1	26.5	26.6	29.2	27.5	24.8	26.2	25.3
Rb	9.51	1.29	0.71	0.28	0.83	1.47	3.41	0.00	1.05	4.17	11.43	0.78	0.71	0.42	1.80	0.70
Sr	1884	2752	2029	2338	1806	1910	1396	4641	3834	3551	3690	1605	1622	1866	1839	1865
Y	0.09	0.29	0.11	0.06	0.03	0.04	0.04	0.18	0.08	0.05	0.06	0.21	0.24	0.19	0.07	0.16
Zr	0.00	0.23	0.00	0.00	0.03	0.10	0.00	0.06	0.00	0.00	0.00	0.01	0.05	0.00	0.05	0.03
Nb	0.04	0.03	0.01	0.04	0.02	0.13	0.03	0.08	0.00	0.01	0.00	0.23	0.18	0.17	0.15	0.15
Cs	0.17	0.18	0.07	0.00	0.07	0.00	0.00	0.00	0.01	0.19	0.63	0.00	0.00	0.03	0.04	0.07
Ba	373	187	186	284	554	308	184	363	907	968	518	250	440	151	125	267
La	9.59	5.73	6.48	6.50	9.67	6.87	4.93	7.51	6.32	4.87	6.78	8.07	6.96	7.64	6.02	8.49
Ce	9.46	7.20	7.32	9.50	10.60	4.79	2.22	9.06	5.99	4.20	7.83	4.89	4.76	4.78	3.22	5.07
Pr	0.50	0.70	0.48	0.68	0.58	0.18	0.09	0.61	0.29	0.32	0.40	0.20	0.19	0.19	0.14	0.20
Nd	0.68	1.83	0.92	1.44	1.71	0.21	0.08	1.82	0.35	0.49	1.49	0.52	0.65	0.24	0.25	0.21
Sm	0.15	0.02	0.00	0.11	0.00	0.00	0.00	0.16	0.00	0.04	0.13	0.00	0.02	0.00	0.00	0.03
Eu	0.86	0.78	0.57	0.82	0.94	0.64	0.18	0.91	0.90	0.61	0.95	0.42	0.72	0.29	0.27	0.46
Gd	0.07	0.08	0.00	0.12	0.06	0.05	0.00	0.07	0.00	0.01	0.03	0.04	0.12	0.02	0.00	0.12
Tb	0.00	0.01	0.00	0.00	0.00	0.00	0.00	0.00	0.00	0.01	0.00	0.00	0.00	0.00	0.00	0.00
Dy	0.05	0.00	0.00	0.00	0.03	0.00	0.00	0.00	0.02	0.10	0.03	0.00	0.00	0.00	0.00	0.00
Ho	0.00	0.01	0.00	0.00	0.00	0.00	0.00	0.01	0.00	0.00	0.01	0.00	0.00	0.00	0.00	0.00
Er	0.00	0.00	0.00	0.00	0.00	0.00	0.00	0.00	0.00	0.00	0.00	0.00	0.00	0.00	0.00	0.00
Tm	0.00	0.00	0.00	0.00	0.00	0.00	0.00	0.00	0.00	0.00	0.00	0.00	0.00	0.00	0.00	0.00
Yb	0.00	0.11	0.02	0.00	0.00	0.04	0.00	0.02	0.00	0.00	0.00	0.00	0.00	0.00	0.00	0.00
Lu	0.00	0.00	0.00	0.00	0.00	0.00	0.00	0.01	0.00	0.00	0.01	0.00	0.00	0.00	0.00	0.00
Hf	0.02	0.00	0.00	0.03	0.00	0.00	0.00	0.00	0.00	0.00	0.01	0.00	0.01	0.01	0.00	0.08
Ta	0.00	0.02	0.02	0.01	0.02	0.19	0.06	0.01	0.00	0.00	0.02	0.34	0.41	0.23	0.29	0.31
Th	0.06	0.34	0.00	0.01	0.00	0.00	0.00	0.05	0.00	0.00	0.01	0.00	0.00	0.04	0.01	0.02
U	0.04	0.10	0.00	0.00	0.00	0.01	0.00	0.02	0.00	0.01	0.02	0.00	0.00	0.02	0.01	0.00

Note: b.d.l. = below detection limit.
[a] Data source: Zhou et al. (2020a).
[b] Data source: This study.

Discussion

Comparison of the magma properties of the three plutons

Magma properties play a key role in the formation of magmatic-hydrothermal ore deposits (Hedenquist and Lowenstern 1994; Audétat and Simon 2012). For example, hydrous, oxidized, and S-rich magmas are favorable for producing porphyry copper systems and associated skarns (Sillitoe 2010, 2018). The Tonglushan, Tieshan, and Jinshandian plutons contain abundant amphibole crystals, which record various intensive parameters and have important implications for magmatic processes (e.g., Zhou et al. 2020b). Several thermobarometers were used to estimate the SiO_2 contents of the melt that was in equilibrium with the crystallizing amphibole crystals and the water content, oxygen fugacity, and temperature of the magmas (Fig. 4) (Ridolfi et al. 2010; Putirka 2016). The results show that the Tonglushan, Tieshan, and Jinshandian amphibole crystals crystallized from melts with SiO_2 contents of 72.4–75.2, 71.6–75.8, and 72.1–78.9 wt%, and in temperature ranges of 725–809, 695–801, and 720–795 °C, respectively. These relatively low-crystallization temperatures and high-silica equilibrium melt, compared to bulk-rock abundances, indicate that the precipitation of amphibole crystals occurred in the late stages during the solidification of the three plutons, consistent with the fact that igneous rocks in the Edong district are the products of an initially water-poor intraplate environment (Wang et al. 2004; Zhou et al. 2020a). A

TABLE 4. Representative amphibole major and trace element compositions

Pluton	Tonglushan[a]					Tieshan[b]						Jinshandian[c]				
Sample			HB008			TS-1	TS-3	HB002	HB004	HB007	HB001		Jsd-2		Jsd-4	
Spot	9	11	21	22	25	132	200	270	79	129	196	1	2	3	133	134
								Oxide contents (wt%)								
SiO_2	50.86	51.13	50.97	50.19	50.61	50.03	50.42	47.92	48.91	48.48	48.05	49.39	49.71	51.78	49.60	50.16
TiO_2	0.77	1.02	0.88	0.94	0.87	0.81	0.70	1.25	1.17	1.20	0.91	0.83	0.88	0.56	1.01	0.85
Al_2O_3	4.73	4.48	4.68	5.02	4.85	5.18	4.29	6.33	5.82	6.06	5.38	4.94	4.58	3.56	3.71	3.54
FeO	11.42	11.45	11.38	11.61	11.34	13.12	13.35	13.44	13.23	13.26	13.13	13.78	13.25	12.05	15.80	15.95
MnO	0.62	0.60	0.54	0.48	0.55	0.38	0.40	0.36	0.47	0.28	0.33	0.18	0.19	0.22	0.33	0.34
MgO	15.56	15.61	15.31	14.93	15.27	13.93	14.22	13.68	13.75	13.79	13.69	14.32	14.71	15.66	12.88	12.91
CaO	11.43	11.70	11.79	12.42	11.67	11.99	11.83	11.56	11.52	11.55	12.06	12.13	12.13	12.38	10.93	11.10
Na_2O	1.23	1.25	1.23	1.23	1.16	1.01	1.22	1.51	1.52	1.60	1.48	1.56	1.49	1.15	2.60	2.50
K_2O	0.49	0.47	0.49	0.53	0.50	0.58	0.51	0.75	0.68	0.69	0.56	0.70	0.70	0.39	0.71	0.78
P_2O_5	b.d.l.	0.02	b.d.l.	b.d.l.	0.02	b.d.l.	0.01	0.01	0.01	0.02	0.03	0.06	b.d.l.	b.d.l.	b.d.l.	b.d.l.
Cr_2O_3	b.d.l.	0.05	0.02	0.02	0.22	0.03	0.04	0.07	0.06	b.d.l.	0.64	0.03	0.06	0.05	0.02	0.01
F	0.26	0.11	0.15	0.25	0.14	0.21	0.35	0.37	0.26	0.35	0.50	b.d.l.	b.d.l.	b.d.l.	0.80	0.87
Cl	0.10	0.13	0.10	0.11	0.12	0.04	0.08	0.06	0.06	0.11	0.08	0.09	0.07	0.05	0.09	0.08
Total	97.33	97.94	97.45	97.59	97.22	97.21	97.25	97.14	97.32	97.20	96.59	97.98	97.76	97.83	98.11	98.70
								Trace element contents (ppm)								
Cu	0.08	0.34	0.18	0.27	0.22	0.53	0.67	0.36	0.32	0.45	1.16	1.85	1.92	1.55	3.32	5.28
Zn	202	175	164	168	170	332	371	308	354	1	324	276	279	274	225	208
Pb	0.65	0.38	1.08	1.63	0.25	1.27	0.88	1.16	2.36	4.19	7.50	0.95	2.04	0.66	0.52	2.30
P	4.2	11.6	20.6	13.5	12.5	11.8	14.3	25.1	9.6	0.0	31.3	12.9	12.1	10.1	11.6	13.5
Li	4.08	4.27	2.29	2.94	3.12	13.2	17.3	11.8	28.3	1.4	86.4	15.0	14.9	13.2	12.1	11.6
Sc	67.9	47.3	70.9	75.7	61.7	58.7	49.2	52.9	61.8	2.4	62.0	67.9	66.7	57.7	162.9	104.7
V	150	138	139	167	141	191	180	220	164	0.11	216	199	189	170	44.0	62.1
Cr	23.1	19.7	17.6	31.3	15.7	32.5	32.6	167	242	1.74	342	170	141	173	4.88	7.24
Co	52.1	53.8	54.2	52.6	53.4	72.0	74.9	61.9	65.3	0.06	48.5	69.5	70.0	68.4	41.5	37.1
Ni	34.5	38.3	36.5	34.7	34.5	72.0	109	75.1	97.4	2.01	96.2	125	126	133	6.26	8.60
Ga	18.7	16.9	17.6	21.5	16.7	23.3	23.1	24.7	19.2	21.5	23.4	22.1	21.3	17.8	32.5	40.2
Rb	4.12	3.55	3.43	5.64	3.03	3.69	4.10	1.81	7.35	0.63	21.19	3.87	3.90	3.29	10.72	15.13
Sr	10.2	11.4	12.7	16.0	12.8	73.6	56.3	42.8	44.3	1633.9	93.8	44.2	44.1	21.8	0.46	7.92
Y	41.7	21.9	26.2	39.1	31.8	12.7	8.36	13.0	11.0	0.03	17.0	8.43	8.38	9.77	360	620
Zr	24.2	20.2	17.6	29.5	18.6	34.6	31.9	45.3	25.6	0.11	42.6	35.6	33.8	41.0	235	165
Nb	17.6	10.4	10.9	21.2	13.1	18.1	5.99	8.38	5.97	0.00	7.95	7.46	7.25	2.76	104	188
Cs	0.06	0.00	0.07	0.20	0.03	0.01	0.01	0.00	0.34	0.01	3.40	0.02	0.03	0.00	0.06	0.01
Ba	3.67	2.26	2.88	6.20	5.00	26.4	11.3	31.8	25.8	340	37.0	12.5	11.82	4.89	0.22	2.58
La	35.8	23.5	26.2	46.8	24.8	37.1	20.2	31.0	15.5	5.6	55.9	25.6	24.4	16.9	40.3	48.0
Ce	94.2	55.2	66.1	112.6	67.2	90.3	39.5	63.0	34.0	3.9	62.4	51.7	47.6	36.1	165	184
Pr	11.9	6.65	8.22	13.49	8.73	12.39	4.05	6.24	4.10	0.16	5.89	5.25	4.85	3.94	26.81	28.97
Nd	53.8	29.5	31.9	52.5	36.9	56.7	16.2	22.4	18.6	0.4	21.9	20.1	18.4	15.3	128	127
Sm	11.8	6.05	7.243	10.6	8.83	9.23	2.96	4.27	3.51	0.00	5.83	3.08	3.22	3.06	49.5	51.4
Eu	1.73	1.15	1.32	1.60	1.44	1.61	0.77	1.06	0.73	0.20	1.16	1.10	1.10	0.68	0.14	0.71
Gd	9.77	5.19	6.14	8.64	7.23	6.09	2.33	3.77	3.17	0.00	4.85	2.68	2.96	2.31	59.5	65.7
Tb	1.36	0.62	0.75	1.13	0.96	0.68	0.24	0.51	0.36	0.00	0.52	0.35	0.30	0.30	11.2	13.9
Dy	6.51	3.86	4.49	6.54	6.24	2.59	1.33	2.20	2.19	0.03	3.02	1.60	1.58	1.40	72.4	96.4
Ho	1.31	0.68	0.83	1.36	1.05	0.40	0.34	0.36	0.35	0.00	0.56	0.33	0.26	0.26	12.7	17.7
Er	4.21	2.54	2.54	3.41	3.07	1.14	0.82	1.30	1.05	0.05	1.84	0.79	0.66	0.96	33.4	48.3
Tm	0.54	0.25	0.33	0.43	0.41	0.12	0.11	0.11	0.09	0.00	0.32	0.08	0.09	0.13	4.16	6.10
Yb	4.17	2.05	2.32	3.75	2.83	0.66	0.69	0.93	1.09	0.00	1.68	0.59	0.81	0.96	26.1	35.7
Lu	0.55	0.32	0.36	0.63	0.43	0.11	0.13	0.16	0.13	0.00	0.32	0.14	0.13	0.17	3.61	4.19
Hf	2.08	1.36	1.11	2.23	1.41	2.32	1.47	2.65	1.90	0.02	2.27	2.04	1.71	2.51	12.9	15.5
Ta	0.18	0.08	0.10	0.20	0.13	0.34	0.04	0.08	0.05	0.00	0.10	0.06	0.04	0.03	2.81	12.05
Th	0.17	0.08	0.10	0.21	0.10	0.38	0.17	0.09	0.07	0.00	2.32	0.07	0.12	0.17	0.26	1.11
U	0.08	0.06	0.05	0.07	0.05	0.07	0.03	0.01	0.04	0.00	2.82	0.03	0.03	0.03	0.03	0.09

Note: b.d.l. = below detection limit.
[a] Data source: Zhou et al. (2020a).
[b] Data source: Zhou et al. (2020a).
[c] Data source: This study.

decrease in SiO_2 contents in equilibrium melts with decreasing temperature (Fig. 4a) suggests that amphibole crystallization was accompanied by quartz crystallization (Fig. 3d). High magmatic water contents are essential for ore deposit genesis because fluid saturation and exsolution are key steps in the mineralization processes (Hedenquist and Lowenstern 1994; Candela 1997; Candela and Piccoli 2005; Zajacz et al. 2008; Audétat and Simon 2012; Wang et al. 2014). Application of the amphibole hygrometer (Ridolfi et al. 2010) shows that the Tonglushan and Tieshan amphibole crystals crystallized from melts with H_2O contents of 3.4–4.4 and 3.2–4.6 wt%, respectively (Fig. 4b; Zhou et al. 2020a). The anhedral amphibole crystals in the Jinshandian pluton record magmatic H_2O contents of 2.9–3.9 wt%, whereas euhedral amphibole crystals crystallized from the melts with H_2O contents of 0.8–2.0 wt% (Fig. 4b). The H_2O contents in the melts that crystallized the Jinshandian euhedral amphibole crystals increased with decreasing temperature, whereas the H_2O contents of the melts that grew the anhedral amphibole in the Jinshandian pluton, as well as amphibole in the Tonglushan and Tieshan, remained approximately constant with cooling (Fig. 4b). In theory, H_2O is incompatible during magma crystallization and will be enriched in residual melts until fluid saturation and exsolution occur. The Jinshandian euhedral amphibole crystals record such a crystallization-dominated trend, whereas the other amphibole trends indicate that fluid exsolution accompanied their crystallization, consistent with higher magmatic water contents and volatile saturation at higher degrees of pluton crystallinity.

Another critical intensive parameter is magmatic oxygen fugacity, which controls the behavior of sulfur as well as metals during magmatic evolution (Audétat and Simon 2012; Richards 2015). High oxygen fugacities are necessary for generating porphyry copper systems, and reduced ilmenite-series intrusions commonly lack economic Cu mineralization (Ishihara 1977, 1981; Sillitoe 2018). The oxidized state of ore-forming magmas is hypothesized to be inherited from subducted oceanic slabs through the transport of slab-derived, oxidized, partial melts or fluids into the mantle wedge, promoting the extraction of metals and sulfur into arc magmas (e.g., Mungall 2002; Evans and Tomkins 2011). In addition, the oxidation state of magmas may also be modified during subsequent magmatic differentiation, leading to either magnetite fractionation-induced oxidation (e.g., Lee et al. 2010) or magnetite fractionation- and degassing-induced reduction (e.g., Jenner et al. 2010; Kelley and Cottrell 2012). The solubility of copper in silicate melts increases with increasing oxygen fugacity (e.g., Zajacz et al. 2012). More importantly, the solubility of sulfur is strongly controlled by the oxidation state of magmas (Baker and Moretti 2011). Oxidized S^{6+} is much more soluble than reduced S^{2+}, and there is a dramatic increase in the sulfur solubility in magmas at magmatic oxygen fugacities greater than ~ΔFMQ+1.0 [corresponding to ~ΔNNO+0.4 at temperatures <1000 °C; Jugo et al. (2010)]. The potential of Cu mineralization is therefore suppressed in magmas with low-oxygen fugacities (e.g., Zajacz et al. 2012). Another possible means of lowering ore-forming potential via low-oxygen fugacities is the sequestration of metals by early sulfide fractionation (e.g., Jenner et al. 2010; Park et al. 2015, 2019; Hao et al. 2017), but this proposal is not widely accepted (e.g., Spooner 1993; Keith et al. 1997; Larocque et al. 2000; Halter

TABLE 5. Representative titanite major and trace element compositions

Pluton	Tonglushan								Jinshandian							
Sample	HB008 (Magmatic)				HB009 (Magmatic)				JSD-4 (Magmatic)					JSD-2 (Secondary)		
Spot	18	s11	s12	s13	s34	s35	s38	s39	138	139	143	145	147	19	20	21
Oxide contents (wt%)																
SiO_2	30.21	31.56	31.12	30.17	30.22	30.53	30.75	30.54	30.42	30.41	30.56	30.41	31.02	30.32	30.56	30.43
TiO_2	37.14	37.65	36.76	35.37	34.50	35.84	36.32	36.21	37.09	36.76	36.86	37.14	35.97	37.01	36.88	36.05
Al_2O_3	0.91	0.98	1.13	1.08	1.31	1.22	1.98	1.23	0.53	0.42	0.67	0.47	0.59	0.78	0.69	1.02
FeO	1.51	1.27	1.49	2.03	2.21	1.95	1.78	1.88	2.43	2.01	1.78	1.82	1.76	1.62	1.42	2.29
MnO	0.09	0.17	0.14	0.24	0.18	0.16	0.14	0.16	b.d.l.	b.d.l.	0.02	0.01	b.d.l.	0.05	0.03	0.07
MgO	0.01	0.02	0.01	0.03	b.d.l.	0.03	0.02	0.03	0.06	0.03	0.05	0.03	0.03	0.03	0.03	0.03
CaO	28.50	27.82	30.25	29.82	30.42	29.19	29.10	29.28	29.15	29.20	29.43	29.66	29.72	29.24	28.99	29.51
Na_2O	b.d.l.	0.01	b.d.l.	0.02	0.06	0.02	b.d.l.	0.05	0.12	0.10	0.11	0.06	0.07	0.04	b.d.l.	b.d.l.
K_2O	b.d.l.	b.d.l.	b.d.l.	b.d.l.	b.d.l.	b.d.l.	0.01	0.02	b.d.l.	b.d.l.	0.02	b.d.l.	b.d.l.	0.02	b.d.l.	b.d.l.
P_2O_5	0.09	0.07	0.05	0.12	0.09	0.07	0.07	0.08	0.08	0.13	0.08	0.11	0.07	0.10	0.09	0.04
Cr_2O_3	b.d.l.	0.04	0.04	b.d.l.	0.06	b.d.l.	0.13	0.01	0.01	b.d.l.	0.01	0.01	0.02	0.03	0.01	0.02
F	b.d.l.	0.12	b.d.l.	b.d.l.	b.d.l.	b.d.l.	b.d.l.	b.d.l.	0.19	0.36	0.17	0.07	0.22	0.22	0.10	0.35
Cl	0.01	b.d.l.	b.d.l.	b.d.l.	0.01	b.d.l.	b.d.l.	b.d.l.	b.d.l.	b.d.l.	0.01	0.01	b.d.l.	b.d.l.	b.d.l.	b.d.l.
Total	98.46	99.66	100.99	98.88	99.05	99.01	100.31	99.48	100.01	99.27	99.69	99.76	99.38	99.36	98.74	99.65
Trace element contents (ppm)																
Cu	2.78	3.61	2.83	2.93	2.53	2.39	3.00	2.70	6.18	5.96	6.28	5.93	6.69	6.12	6.44	6.03
Zn	7.31	7.86	6.09	13.52	5.70	6.05	6.79	5.09	12.3	12.4	12.3	11.5	13.3	12.3	12.2	13.4
Pb	7.48	3.45	3.19	15.57	8.02	5.48	4.82	5.16	4.71	4.97	5.23	4.59	9.42	6.15	8.74	9.31
P	243	163	168	517	312	273	342	268	209	248	254	262	382	413	329	291
Sc	14.8	12.9	13.0	21.8	24.6	19.2	15.9	18.2	17.3	16.6	25.5	25.4	25.4	12.3	10.9	12.5
V	660	591	566	597	767	668	614	629	598	598	550	523	698	673	745	670
Cr	9.77	13.7	12.6	18.4	17.5	14.5	18.1	18.3	11.9	8.92	5.55	5.58	6.20	139	188	87
Co	0.20	0.08	0.07	0.73	0.11	0.12	0.12	0.12	0.12	0.08	0.09	0.04	0.11	0.16	0.09	0.18
Rb	1.05	0.43	0.08	3.11	0.86	0.31	0.24	0.31	0.87	0.98	0.39	0.37	0.51	0.61	0.17	0.18
Sr	10.3	22.4	21.9	17.5	44.0	42.4	42.8	38.9	47.0	49.7	65.4	67.0	72.0	76.5	74.9	71.2
Y	2263	778	797	2720	4352	1898	1342	1355	2070	2248	920	902	1219	259	451	535
Zr	693	343	347	2324	1478	1051	643	924	3068	3603	3929	3884	2434	962	763	791
Nb	1857	560	565	3864	2843	1596	1480	1256	2586	2959	1847	1929	2917	797	1018	1540
Ba	0.38	0.31	0.04	2.23	0.09	0.09	0.08	0.03	0.00	0.03	0.04	0.02	0.73	0.32	0.06	0.31
La	5502	1681	1724	7628	4512	3828	3445	3671	1125	1317	1522	1421	2140	2974	3242	4245
Ce	12816	3852	3879	16239	14768	10883	9540	9780	4384	5071	3029	2899	4914	4932	6781	9261
Pr	1372	436	444	1743	2095	1325	1099	1089	605	687	288	282	475	399	672	961
Nd	5126	1665	1700	6302	8645	4537	3601	3539	2629	2898	1073	1052	1663	1141	2475	3441
Sm	890	269	276	1001	1405	565	433	413	567	618	201	191	284	124	337	458
Eu	120	67.0	65.7	147	206	141	111	117	29.2	33.8	25.1	25.7	41.3	108	96.2	131
Gd	643	219	218	786	1039	380	287	274	487	519	184	175	252	88.2	224	295
Tb	79.9	26.6	27.1	98.7	142	51.6	36.7	36.4	66.5	72.2	25.1	23.9	33.8	8.77	21.3	26.5
Dy	445	136	140	514	782	288	203	199	396	426	156	150	213	45.5	98.4	119
Ho	79.2	28.1	28.3	99.4	156	59.7	41.9	41.2	71.6	78.5	30.9	29.7	40.5	7.7	15.1	19.0
Er	226	71.4	73.8	261	425	175	122	125	207	225	93.5	89.3	127	23.0	42.6	49.0
Tm	30.2	10.5	10.9	39.0	63.7	29.0	20.3	21.2	28.0	31.2	13.6	13.2	17.6	3.21	5.24	5.94
Yb	219	66.2	66.7	236	367	185	129	140	186	205	94.3	90.7	127	25.5	34.9	41.3
Lu	29.1	9.95	10.4	34.2	46.7	26.3	19.4	20.6	23.2	24.7	13.9	12.7	18.5	3.74	4.76	5.71
Hf	55.5	24.0	25.5	291	99.8	90.5	39.1	77.6	89.0	89.3	164	180	98.0	50.2	51.3	60.3
Ta	77.4	14.2	13.7	332	227	106	83.2	69.0	203	211	98.5	107	109	25.9	35.1	44.1
Th	517	261	265	1040	649	418	343	386	430	468	496	429	738	438	622	684
U	289	93.7	89.5	382	61.4	44.3	38.5	42.6	26.3	31.7	44.7	42.7	97.6	106	148	104

Notes: b.d.l. = below detection limit. Data source for all is this study.

TABLE 6. Representative apatite major and trace element compositions

Pluton	Tonglushan				
Sample	HB008			HB009	
Spot	s15	s16	s17	s29	s30
	Oxide contents (wt%)				
SiO_2	0.21	0.05	b.d.l.	b.d.l.	0.24
TiO_2	b.d.l.	b.d.l.	0.07	0.03	b.d.l.
Al_2O_3	b.d.l.	0.00	b.d.l.	0.01	b.d.l.
FeO	0.09	0.08	0.02	0.06	0.06
MnO	0.10	0.10	0.06	0.14	0.11
MgO	0.01	b.d.l.	0.01	b.d.l.	0.00
CaO	54.72	54.93	55.35	54.87	54.65
Na_2O	0.00	0.02	0.09	0.07	0.05
K_2O	b.d.l.	b.d.l.	b.d.l.	0.01	0.01
P_2O_5	42.80	42.39	42.46	42.36	41.63
Cr_2O_3	0.01	b.d.l.	b.d.l.	b.d.l.	b.d.l.
F	3.20	3.49	3.46	2.85	3.11
Cl	0.37	0.30	0.23	0.50	0.59
Total	100.08	99.82	100.24	99.57	99.01
	Trace element contents (ppm)				
Cu	0.70	0.59	0.34	0.36	0.50
Zn	0.51	0.40	0.12	0.54	0.34
Pb	1.54	1.38	1.18	1.03	2.41
V	11.3	10.19	9.48	10.8	17.2
Rb	0.02	0.05	0.02	0.00	0.17
Sr	504	509	511	432	431
Y	199	153	148	156	403
Zr	1.11	0.44	0.45	0.35	2.47
Ba	0.31	0.26	0.10	0.14	0.25
La	2635	2125	2037	1726	3959
Ce	3183	2532	2415	2248	5307
Pr	254	200	190	193	466
Nd	754	580	555	602	1469
Sm	86.9	65.2	62.0	72.2	184
Eu	17.5	13.3	12.8	10.6	26.3
Gd	154	121	114	109	265
Tb	6.63	5.05	4.54	5.34	14.33
Dy	33.8	24.8	23.8	26.9	69.1
Ho	6.51	4.88	4.61	5.01	13.49
Er	18.1	13.4	12.9	14.0	35.3
Tm	2.39	1.81	1.63	1.61	4.36
Yb	14.1	11.5	10.5	10.2	27.0
Lu	2.78	2.00	1.94	1.74	4.72
Th	65.3	65.3	62.2	45.2	177
U	14.0	23.5	24.6	14.4	55.2

Notes: b.d.l. = below detection limit. Data source for all is this study.

et al. 2002, 2005; Stavast et al. 2006; Nadeau et al. 2010, 2013; Wilkinson 2013; Du and Audétat 2020). Here, we employed the amphibole oxybarometer (Ridolfi et al. 2010) to track the oxidation state of the three plutons. As illustrated in Figures 4c and 4d, the amphibole crystals in the Tonglushan, Tieshan, and Jinshandian plutons record magmatic oxygen fugacities ranging from ΔNNO+1.0 to ΔNNO+2.5, ΔNNO+1.0 to ΔNNO+2.2 (Zhou et al. 2020a; Duan and Jiang 2017), and ΔNNO+0.9 to ΔNNO+2.1, respectively. Thus, there is no systematic difference in magmatic oxygen fugacity between Cu and Cu-poor Fe mineralizing magmas. However, it is noteworthy that the oxygen fugacities of euhedral amphibole crystals in the Jinshandian pluton decrease with cooling, whereas those of other amphibole crystals increase with decreasing temperature (Fig. 4d). Combined with the evolving trends of water, we can speculate that magmatic oxygen fugacities will decrease with crystallization but increase with crystallization accompanying fluid exsolution.

The efficiency of copper extraction

The significant enrichment of Cu from magmas with normal concentrations of Cu (~50–100 ppm) (Cline and Bodnar 1991; Richards 2015; Chelle-Michou et al. 2017; Zhang and Audétat 2017) to anomalously Cu-rich fluids (Audétat 2019) may be described by fluid separation due to very high fluid/melt partition coefficients (Zajacz et al. 2008; Audétat 2019). Assuming that the common factors such as sulfur contents, host rocks and depths are beneficial for mineralization, fluid exsolution can be observed in many shallow intrusions but only a small portion of these produce Cu mineralization, suggesting that there are other factors that downgrade the Cu mineralization potential of a barren intermediate-felsic intrusion. The intermediate-felsic intrusions represent residual material after fluid exsolution and therefore offer clues to the mineralization potential of a given system.

For this purpose, we present a systematic comparison of the compositions of common minerals in the Tonglushan, Tieshan, and Jinshandian plutons, including clinopyroxene, plagioclase, K-feldspar, amphibole, titanite, and apatite. Two important factors should be addressed before such comparisons: (1) exclusion of data that were contaminated by crystal, melt, and fluid inclusions; and (2) establishing the influence of disequilibrium zoning patterns (such as sector zoning) on mineral compositions. Small crystals, melt, and/or fluid inclusions are easily trapped by large crystals during magmatic crystallization (e.g., Halter et al. 2004), and their presence may affect microanalyses. Examination of the transient signals from analyses is a useful approach for identifying fine-scale inclusions in minerals. All microanalytical data for mineral Cu content was checked for transient signals and the data showing the presence of inclusions were excluded. Another problem is the influence of the zoning patterns that were produced by disequilibrium crystal growth. Unlike commonly observed equilibrium zonation in igneous crystals such as normal, reverse and oscillatory zoning patterns, sector zoning is a kinetically induced compositional zoning in, which compositionally heterogeneous domains might have crystallized from the same melt at similar conditions (e.g., Zhou et al. 2021). An example of its influence on mineral compositions is provided by titanite from the Tonglushan pluton (Fig. 5). Titanite ($CaTiSiO_5$) is a common Ti-bearing accessory phase in granitoid rocks (e.g., Piccoli et al. 2000) and hydrothermal systems (e.g., Chelle-Michou et al. 2015; Song et al. 2019) and has very high contents of certain trace elements (e.g., REE, Y, Zr, Nb, U, Th, etc.). Due to low-cation diffusivities, titanite commonly develops sector zoning, even at relatively low crystal growth rates (Paterson and Stephens 1992; Watson and Liang 1995; Kohn 2017). In metaluminous granitoids, the crystal habit of titanite is dominated by {111} (Paterson and Stephens 1992). Exactly which faces are cut depends on the angle at which the plane of the thin section intersects the grain, and the resulting zoning patterns are diverse and complex. In general, the dominant {111} sectors have lower grayscale values in backscattered electron (BSE) images and lower REE, Zr, U, Pb, Nb, and Y contents relative to non-{111} sectors (Paterson and Stephens 1992; Kohn 2017). The results of this study show that non-{111} sectors have higher P, Y, Zr, Nb, Ta, REE, Pb, and U contents than those of {111} sectors by factors of ~2.5, ~2, ~3, ~5, ~6, ~2, ~3, and ~5, respectively. However, there is no pronounced difference in Cu contents among different sectors. For example, in the titanite crystal in Figure 5b, the average Cu contents of the {111} and non-{111} sectors are 2.70 and 2.21 ppm, respectively. Although there is no experimentally determined diffusivity of Cu in titanite to date (Kohn 2017), high values may be inferred because the low valence of Cu facilitates its diffusion in minerals compared to most other elements (Audétat et al. 2018). The lack of obvious differences in Cu content among different sectors in titanite may be ascribed to the low ratios of growth rate to lattice diffusivity (Watson and Liang 1995). Thus, our results indicate that the influence of disequilibrium zoning on titanite Cu contents is limited. Disequilibrium zoning has not been observed in other minerals.

The above assessment demonstrates that it is possible to make meaningful comparisons between the mineral compositions of the Tonglushan, Tieshan, and Jinshandian plutons. A systematic comparison of mineral Cu concentrations of the three plutons is illustrated in Figure 6 and Table 7. The result shows that almost all minerals in the Jinshandian pluton have higher Cu contents than those in the Tonglushan and Tieshan plutons. The Tonglushan deposit contains 1.08 Mt Cu and the Tieshan deposit contains 0.67 Mt Cu, but no economic Cu ore body has been found in the Jinshandian deposit. It is unlikely that the parental magmas of the Jinshandian pluton are more Cu-rich than those of the Tonglushan and Tieshan plutons. Higher mineral Cu contents may also be attributed to higher partition coefficients of Cu between mineral and melt. However, it is implausible that all minerals in the Jinshandian pluton have higher mineral-melt partition coefficients of Cu at the same time. Thus, systematically lower mineral Cu contents of the Cu- mineralized plutons should be ascribed to Cu being extracted from these plutons by exsolved fluids more efficiently and completely.

Possible factors that affect the Cu-mineralizing potential

At the transition from magmatic to hydrothermal processes, a key factor responsible for the lack of economic mineralization in barren plutons is inefficient fluid exsolution and extraction during their solidification (e.g., Zhang and Audétat 2018). On the basis of our comparison of the three skarn associated plutons, which all underwent efficient fluid exsolution and extraction, this study presents evidence that the minerals in Cu mineralizing plutons have distinctly lower Cu concentrations and show more efficient copper extraction relative to Cu-poor Fe mineralizing plutons. Our results are consistent with observations in certain other porphyry copper systems. For example, in the Los Bronces-Río Blanco district (central Chile), the most productive porphyry Cu province in the world (Sillitoe 2012), plagioclase phenocrysts from fertile porphyries contain significantly lower Cu contents (~0.5 ppm) than those from barren intrusions (~6 ppm) (Williamson et al. 2016). Collectively, these results demonstrate that the efficiency of copper extraction from magmas plays a critical role in determining Cu mineralization potential (e.g., Cline and Bodnar 1991; Richards 2015; Chelle-Michou et al. 2017; Zhang and Audétat 2017). More significantly, extensive skarn alteration also developed around the Cu-poor Jinshandian Fe mineralized pluton, excluding the possibility that the lower efficiency of Cu extraction from the Jinshandian pluton was caused by inefficient fluid exsolution and extraction. It is also unlikely that the initial Cu contents of the Jinshandian pluton are

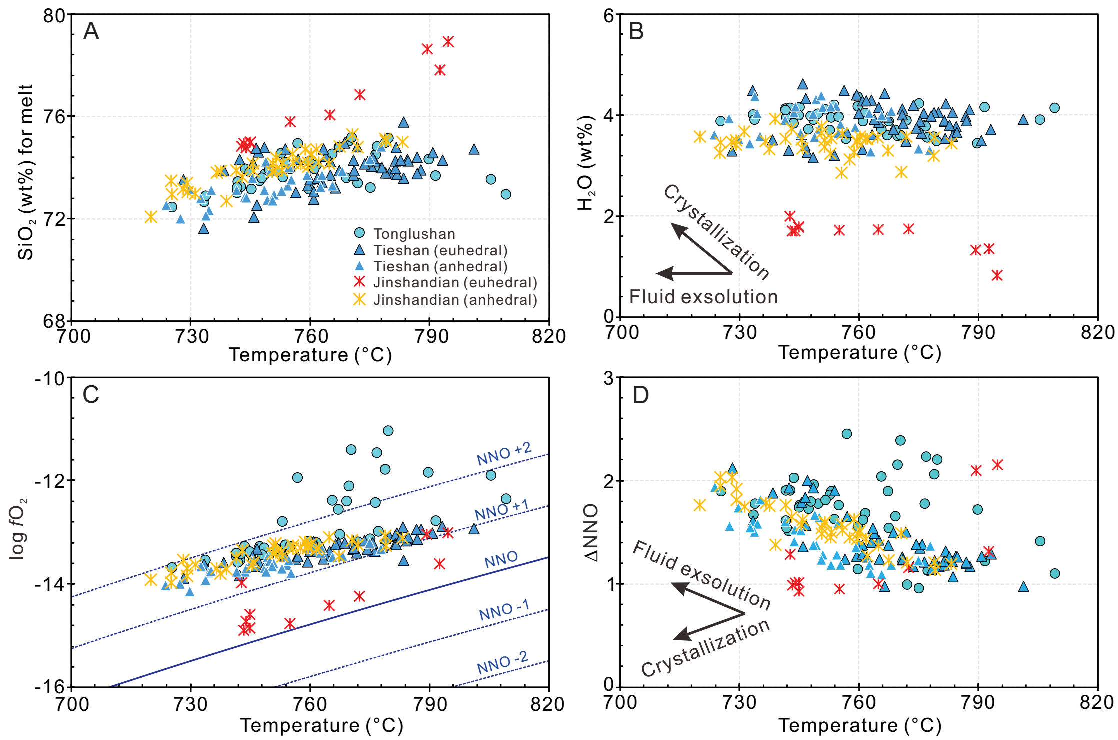

Figure 4. (**a**) Plot of SiO_2 contents in equilibrium with amphiboles vs. temperatures. Equations 5 and 10 from Putirka (2016) were employed to estimate temperature and equilibrium melt SiO_2 contents. (**b**) Magmatic water contents vs. temperatures. Equation 3 of Ridolfi et al. (2010) was used to calculate water content, and Equation 5 of Putirka (2016) was employed to estimate temperature. (**c** and **d**) Magmatic oxygen fugacities vs. temperatures. Equation 2 of Ridolfi et al. (2010) was used to calculate oxygen fugacity, and Equation 5 of Putirka (2016) was employed to estimate temperature. The calibrations of the nickel-nickel oxide (NNO) buffer are taken from O'Neill and Pownceby (1993). (Color online.)

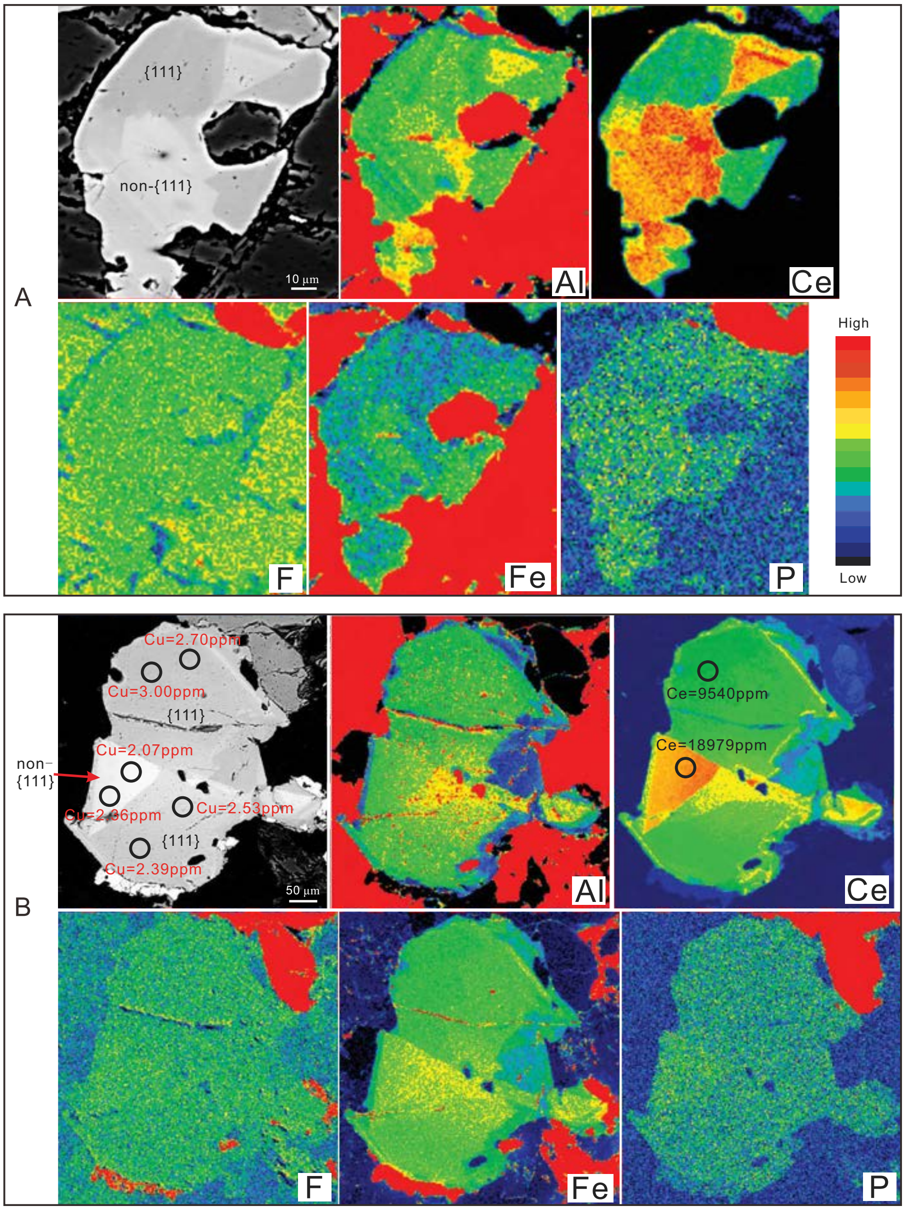

Figure 5. BSE and X-ray mapping images of two euhedral, magmatic titanite crystals with sector zoning. They are from the Tonglushan pluton. Cu and Ce concentrations are marked in different sectors of crystal (**b**). (Color online.)

higher than those of the other Cu-mineralized plutons. There must have been other factors that downgraded the Cu-mineralizing potential of the Jinshandian pluton.

Here we present two possible explanations for inefficient copper extraction during the solidification of the Jinshandian pluton. Anionic ligands are required to transport Cu from magmas into hydrothermal fluids, and chloride complexes are conventionally regarded as the dominant carrier of Cu in aqueous fluids (e.g., Holland 1972; Burnham 1967, 1997; Burnham and Ohmoto 1980; Candela and Holland 1984). Abundant Fe skarn ore bodies around the Jinshandian pluton indicate no shortage of the chloride anion (Cl^-) in the exsolving fluids because iron is transported as chloride complexes in aqueous fluids (e.g., Simon et al. 2004; Zajacz et al. 2008), as also evidenced by halogen-bearing minerals such as scapolite and amphibole in the Jinshandian skarns (Zhu et al. 2015). In addition, many ore bodies in the Jinshandian deposit are distributed within the endoskarns (Zhu et al. 2017) whose protoliths are igneous rocks (Meinert et al. 2005), indicating that Cl^- was derived from the intrusion rather than from the evaporate-bearing country rocks. Thus, the inefficient transport of Cu from magmas into fluids is unlikely a result of a lack of Cl^- in parent magmas. Experimental studies suggest that sulfur plays an important role in the transport of Cu from melts into alteration-mineralization zones, particularly in exsolving magmatic vapors (e.g., Zajacz et al. 2008, 2011; Seo et al. 2009; Zajacz and Halter 2009). It raises the possibility that the lower efficiency of copper transfer from magmas into fluids or vapors may be affected by sulfur. H_2S may increase Cu partitioning between felsic melts and fluids; however, SO_2 has a weak effect on Cu partitioning (Tattitch and Blundy 2017). Thus,

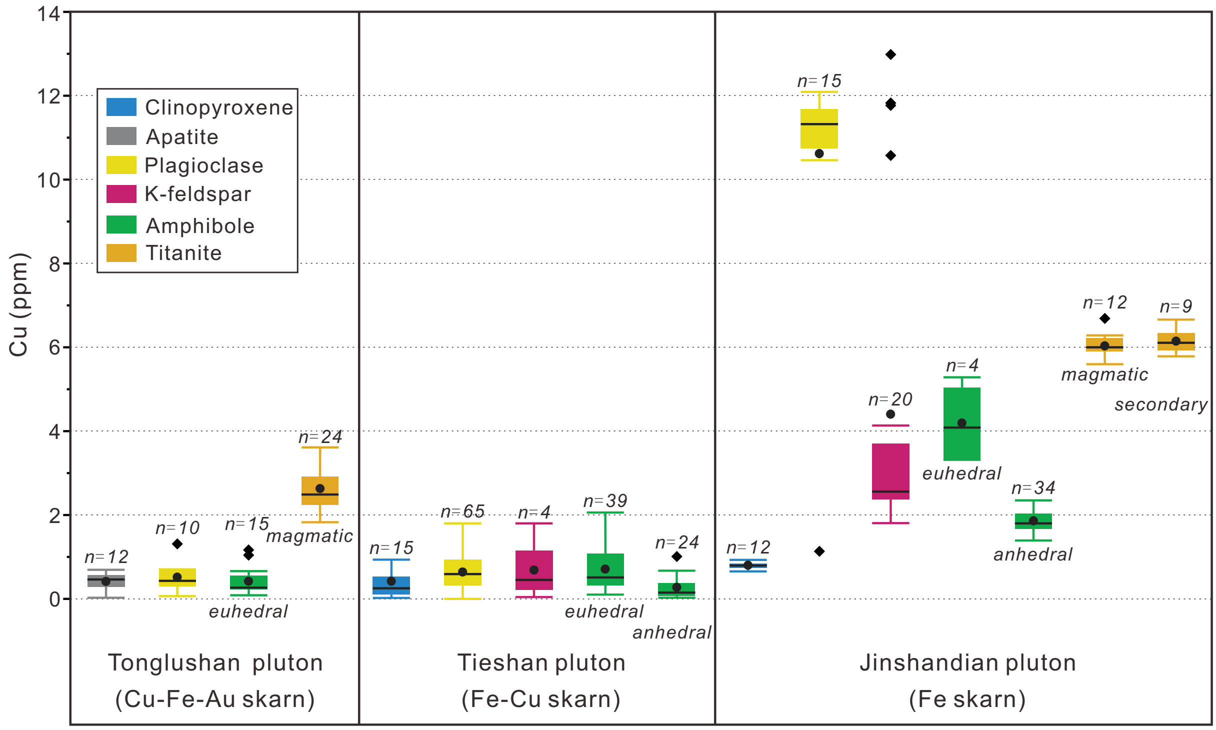

FIGURE 6. Box-whisker plots of mineral Cu concentrations for the Tonglushan, Tieshan, and Jinshandian plutons. Number of analyses is marked above each box plot. The top and bottom of the boxes are the first and second quartiles. The black line is the median, and the full circle is the average. The whiskers represent the values within 1.5 times the interquartile range beyond the box edges. The full rhombuses represent outliers. (Color online.)

the lack of reduced S species during fluid exsolution potentially suppresses the extraction of Cu from parent magmas. However, a decrease in fluid-melt Cu partition coefficients caused by the lack of H_2S is still limited (Tattitch and Blundy 2017). Recent studies emphasized that Cu will be extracted efficiently by hypersaline liquid at low pressures and high temperatures (Blundy et al. 2021; Tattitch et al. 2021), and Cu mineralization preferentially occurs when both Cu and Cl are enriched in residual magmas concurrently (Tattitch et al. 2021). Thus, another possible explanation is that Cu and Cl evolved along different paths during the solidification of the Jinshandian pluton, and one of them was depleted at the point of fluid saturation.

TABLE 7. Comparison of the Tonglushan, Tieshan, and Jinshandian plutons

	Tonglushan		Tieshan		Jinshandian	
Deposit style	Skarn		Skarn		Skarn	
Metals	Cu-Fe-Au		Fe-Cu		Fe	
	Range	Mean	Range	Mean	Range	Mean
			Magma properties			
Whole-rock SiO_2	62.6–63.7		62.4–64.7		68.2–69.3	
Whole-rock Sr/Y	54–56		88–169		5–18	
Amp(euh) *T* (°C)	725–809	760 ± 19	728–801	768 ± 16	743–795	763 ± 21
Amp(anh) *T* (°C)			695–778	747 ± 17	720–783	751 ± 16
Amp(euh) H_2O (wt%)	3.4–4.4	3.9 ± 0.2	3.2–4.6	3.9 ± 0.4	1.3–2.0	1.6 ± 0.3
Amp(anh) H_2O (wt%)			3.3–4.4	3.8 ± 0.3	2.9–3.9	3.5 ± 0.2
Amp(euh) f_{O_2}	1.0–2.5	1.7 ± 0.3	1.0–2.1	1.4 ± 0.3	0.9–2.1	1.3 ± 0.4
Amp(anh) f_{O_2}			1.1–2.2	1.5 ± 0.3	1.1–2.0	1.6 ± 0.2
			Mineral Cu contents (ppm)			
Cpx			0.02–0.94	0.36 ± 0.29	0.65–0.93	0.80 ± 0.08
Ap	0.03–0.70	0.41 ± 0.21				
Pl	0.06–1.31	0.52 ± 0.34	0.03–1.80	0.64 ± 0.42	1.13–12.09	10.6 ± 2.7
Kfs			0.04–1.80	0.69 ± 0.77	1.81–13.0	4.40 ± 3.84
Amp(euh)	0.08–1.15	0.42 ± 0.32	0.10–2.06	0.71 ± 0.52	3.32–5.28	4.19 ± 1.00
Amp(anh)			0.03–1.01	0.28 ± 0.26	1.85–2.23	1.86 ± 0.25
Ttn(mag)	1.83–3.61	2.61 ± 0.50			5.59–6.69	6.03 ± 0.30
Ttn(sec)					5.78–6.66	6.14 ± 0.28

Note: Mineral abbreviations: Amp(euh) = euhedral amphibole; Amp(anh) = anhedral amphibole; Cpx = clinopyroxene; Ap = apatite; Pl = plagioclase; Kfs = K-feldspar; Ttn(mag) = magmatic titanite; Ttn(sec) = secondary titanite.

Implications

This study presents a comparison of three contrasting types of mineralization associated with plutons in the Edong district, where two plutons are related to Cu mineralization, and the other is a Cu-poor, Fe mineralized pluton. Extensive skarn alteration around the three plutons shows that efficient fluid exsolution occurred during their solidification. The three plutons had similar oxygen fugacities (within a range of ~ΔNNO+0.9 to ΔNNO+2.5). Almost all minerals in the Cu mineralizing plutons have lower Cu concentrations than those of the Cu-poor Fe mineralizing pluton, indicating the Cu mineralizing plutons underwent more efficient copper extraction. Thus, the efficiency of copper extraction from magmas plays a critical role in determining Cu mineralization potential. Our results indicate that a variety of igneous minerals with anomalously low Cu contents could potentially be used as a tool to identify a Cu mineralizing magma body in a deposit with multiphase intrusions; nevertheless, a suite of igneous mineral compositions from a region should be analyzed for comparison. Our results suggest that the inefficient copper extraction from magma body may be ascribed to the lack of reduced S species during fluid exsolution or different evolution paths of Cu and Cl during magma crystallization.

Acknowledgments

We are grateful to Associate Editor Callum J. Hetherington, Brian Tattitch, and two anonymous reviewers for helpful, insightful, and constructive reviews, and Editor Don R. Baker for efficient editorial handling. We thank Lin-Li Chen and Chang-Ming Xing for laboratory assistance, and Jun Wang for field help.

Funding

This research was supported by the National Natural Science Foundation of China (No. 42021002). This is Contribution No.IS-3222 from GIGCAS.

References cited

Arndt, N.T., Fontboté, L., Hedenquist, J.W., Kesler, S.E., Thompson, J.F., and Wood, D.G. (2017) Future global mineral resources. Geochemical Perspectives, 6, 1–171.

Audétat, A. (2015) Compositional evolution and formation conditions of magmas and fluids related to porphyry Mo mineralization at Climax, Colorado. Journal of Petrology, 56, 1519–1546.

——— (2019) The metal content of magmatic-hydrothermal fluids and its relationship to mineralization potential. Economic Geology, 114, 1033–1056.

Audétat, A., and Pettke, T. (2003) The magmatic-hydrothermal evolution of two barren granites: a melt and fluid inclusion study of the Rito del Medio and Cañada Pinabete plutons in northern New Mexico (U.S.A.). Geochimica et Cosmochimica Acta, 67, 97–121.

Audétat, A., and Simon, A.C. (2012) Magmatic controls on porphyry copper genesis. In J.W. Hedenquist, M. Harris, and F. Camus, Eds., Geology and Genesis of Major Copper Deposits and Districts of the world: A Tribute to Richard H. Sillitoe. Society of Economic Geologists, Special Publication 16, 553–572.

Audétat, A., Zhang, L., and Ni, H. (2018) Copper and Li diffusion in plagioclase, pyroxenes, olivine and apatite, and consequences for the composition of melt inclusions. Geochimica et Cosmochimica Acta, 243, 99–115.

Baker, D.R., and Moretti, R. (2011) Modeling the solubility of sulfur in magmas: A 50-year old geochemical challenge. Reviews in Mineralogy and Geochemistry, 73, 167–213.

Blundy, J., Mavrogenes, J., Tattitch, B., Sparks, S., and Gilmer, A. (2015) Generation of porphyry copper deposits by gas–brine reaction in volcanic arcs. Nature Geoscience, 8, 235–269.

Blundy, J., Afanasyev, A., Tattitch, B., Sparks, S., Melnik, O., Utkin, I., and Rust, A. (2021) The economic potential of metalliferous sub-volcanic brines. Royal Society Open Science, 8, 202192.

Burnham, C.W. (1967) Hydrothermal fluids at the magmatic stage. In H.L. Barnes, Ed., Geochemistry of Hydrothermal Ore Deposits. Holt, Rinehart and Winston, p. 34–76.

——— (1997) Magmas and hydrothermal fluids. In H.L. Barnes, Ed., Geochemistry of Hydrothermal Ore Deposits, 3rd ed., p. 63–123. Wiley.

Burnham, C.W., and Ohmoto, H. (1980) Late-stage processes of felsic magmatism: Mining Geology. Special Issue, 1–11.

Candela, P.A. (1997) A review of shallow, ore-related granites: Textures, volatiles, and ore metals. Journal of Petrology, 38, 1619–1633.

Candela, P.A., and Holland, H.D. (1984) The partitioning of copper and molybdenum between silicate melts and aqueous fluids. Geochimica et Cosmochimica Acta, 48, 373–380.

Candela, P.A., and Piccoli, P.M. (2005) Magmatic processes in the development of porphyry-type ore systems. In J.W. Hedenquist, J.F.H. Thompson, R.J. Goldfarb, and J.P.,Richards, Eds., Economic Geology 100th Anniversary Volume, 25–37. Society of Economic Geologists, Littleton, Colorado.

Cao, M.J., Hollings, P., Cooke, D.R., Evans, N.J., McInnes, B.I.A., Qin, K.Z., Li, G.M., Sweet, G., and Baker, M. (2018) Physicochemical processes in the magma chamber under the Black Mountain porphyry Cu-Au deposit (Philippines): Insights from mineral chemistry and implications for mineralization. Economic Geology, 113, 63–82.

Chang, Z., Shu, Q., and Meinert, L.D. (2019) Skarn Deposits of China. In Z. Chang and R.J. Goldfarb, Eds., Mineral deposits of China. Society of Economic Geologists, Special Publication 22, 189–234.

Chelle-Michou, C., Chiaradia, M., Selby, D., Ovtcharova, M., and Spikings, R.A. (2015) High-resolution geochronology of the coroccohuayco porphyry-skarn deposit, Peru: A rapid product of the incaic orogeny. Economic Geology, 110, 423–443.

Chelle-Michou, C., Rottier, B., Caricchi, L., and Simpson, G. (2017) Tempo of magma degassing and the genesis of porphyry copper deposits. Scientific Reports, 7, 40566.

Chen, H.Y., Zhang, S.T., Chu, G.B., Zhang, Y., Cheng, J.M., Tian, J., and Han, J.S. (2019) The short wave infrared (SWIR) spectral characteristics of alteration minerals and applications for ore exploration in the typical skarn-porphyry deposits, Edong ore district, eastern China. Acta Petrologica Sinica, 35, 3629–3643. (In Chinese with English abstract.)

Chiaradia, M. (2014) Copper enrichment in arc magmas controlled by overriding plate thickness. Nature Geoscience, 7, 43–46.

Chiaradia, M., and Caricchi, L. (2017) Stochastic modelling of deep magmatic controls on porphyry copper deposit endowment. Scientific Reports, 7, 44523.

Cline, J.S., and Bodnar, R.J. (1991) Can economic porphyry copper mineralization be generated by a typical calc-alkaline melt? Journal of Geophysical Research, 96, 8113–8126.

Cooke, D.R., Hollings, P., and Walshe, J.L. (2005) Giant porphyry deposits: Characteristics, distribution, and tectonic controls. In J.W. Hedenquist, J.F.H. Thompson, R.J. Goldfarb, and J.P. Richards, Eds., Economic Geology 100th Anniversary Volume, 801–888. Society of Economic Geologists, Littleton, Colorado.

Davidson, J., Turner, S., and Plank, T. (2013) Dy/Dy*: Variations arising from mantle sources and petrogenetic processes. Journal of Petrology, 54, 525–537.

Du, J., and Audétat, A. (2020) Early sulfide saturation is not detrimental to porphyry Cu-Au formation. Geology, 48, 519–524.

Duan, D., and Jiang, S. (2017) In situ major and trace element analysis of amphiboles in quartz monzodiorite porphyry from the Tonglvshan Cu–Fe (Au) deposit, Hubei Province, China: Insights into magma evolution and related mineralization. Contributions to Mineralogy and Petrology, 172, 36.

Evans, K., and Tomkins, A.G. (2011) The relationship between subduction zone redox budget and arc magma fertility. Earth and Planetary Science Letters, 308, 401–409.

Halter, W.E., Pettke, T., and Heinrich, C.A. (2002) The origin of Cu/Au ratios in porphyry-type ore deposits. Science, 296, 1844–1846.

Halter, W.E., Heinrich, C.A., and Pettke, T. (2004) Laser-ablation ICP-MS analysis of silicate and sulfide melt inclusions in an andesitic complex II: evidence for magma mixing and magma chamber evolution. Contributions to Mineralogy and Petrology, 147, 397–412.

——— (2005) Magma evolution and the formation of porphyry Cu-Au ore fluids: Evidence from silicate and sulfide melt inclusions. Mineralium Deposita, 39, 845–863.

Hao, H., Campbell, I.H., Park, J.-W., and Cooke, D.R. (2017) Platinum-group element geochemistry used to determine Cu and Au fertility in the Northparkes igneous suites, New South Wales, Australia. Geochimica et Cosmochimica Acta, 216, 372–392.

Hedenquist, J.W., and Lowenstern, J.B. (1994) The role of magmas in the formation of hydrothermal ore deposits. Nature, 370, 519–527.

Hedenquist, J.W., Arribas, A., and Reynolds, T.J. (1998) Evolution of an intrusion-centered hydrothermal system; Far Southeast-Lepanto porphyry and epithermal Cu-Au deposits, Philippines. Economic Geology, 93, 373–404.

Holland, H.D. (1972) Granites, solutions, and base metal deposits. Economic Geology, 67, 281–301.

Hou, Z.Q., Pan, X.F., Li, Q.Y., Yang, Z.M., and Song, Y.C. (2013) The giant Dexing porphyry Cu-Mo-Au deposit in east China, product of melting of juvenile lower crust in an intracontinental setting. Mineralium Deposita, 48, 1019–1045.

Hou, Z., Yang, Z., Lu, Y., Kemp, A.I., Zheng, Y., Li, Q., Tang, J., Yang, Z., and Duan, L. (2015) A genetic linkage between subduction- and collision-related porphyry Cu deposits in continental collision zones. Geology, 43, 247–250.

Hu, X., Chen, H., Zhao, L., Han, J., and Xia, X. (2017) Magnetite geochemistry of the Longqiao and Tieshan Fe–(Cu) deposits in the Middle-Lower Yangtze

River Belt: Implications for deposit type and ore genesis. Ore Geology Reviews, 89, 822–835.
Ishihara, S. (1977) The magnetite-series and ilmenite-series granitic rocks. Mining Geology, 27, 293–305.
——— (1981) The granitoid series and mineralization. In B.J. Skinner, Ed., Economic Geology 75th Anniversary Volume, 458–484.
Jenner, F.E., O'Neill, H.St.C., Arculus, R.J., and Mavrogenes, J.A. (2010) The magnetite crisis in the evolution of arc-related magmas and the initial concentration of Au, Ag and Cu. Journal of Petrology, 51, 2445–2464.
Jugo, P.J., Wilke, M., and Botcharnikov, R.E. (2010) Sulfur *K*-edge XANES analysis of natural and synthetic basaltic glasses: Implications for S speciation and S content as function of oxygen fugacity. Geochimica et Cosmochimica Acta, 74, 5926–5938.
Keith, J.D., Whitney, J.A., Hattori, K., Ballantyne, G.H., Christiansen, E.H., Barr, D.L., Cannan, T.M., and Hook, C.J. (1997) The role of magmatic sulfides and mafic alkaline magmas in the Bingham and Tintic mining districts, Utah. Journal of Petrology, 38, 1679–1690.
Kelley, K.A., and Cottrell, E. (2012) The influence of magmatic differentiation on the oxidation state of Fe in a basaltic arc magma. Earth and Planetary Science Letters, 329-330, 109–121.
Kohn, M.J. (2017) Titanite petrochronology. Reviews in Mineralogy and Geochemistry, 83, 419–441.
Larocque, A.C.L., Stimac, J.A., Keith, J.D., and Huminicki, M.A.E. (2000) Evidence for open-system behavior in immiscible Fe-S-O liquids in silicate magmas: Implications for contributions of metals and sulfur to ore-forming fluids. Canadian Mineralogist, 38, 1233–1249.
Lee, C.A., Luffi, P., Roux, V.L., Dasgupta, R., Albarede, F., and Leeman, W.P. (2010) The redox state of arc mantle using Zn/Fe systematics. Nature, 468, 681–685.
Lee, C.A., Luffi, P., Chin, E.J., Bouchet, R.A., Dasgupta, R., Morton, D.M., Roux, V.L., Yin, Q., and Jin, D. (2012) Copper Systematics in Arc Magmas and Implications for Crust-Mantle Differentiation. Science, 336, 64–68.
Li, X.H., Li, Z.X., Zhou, H.W., Liu, Y., and Kinny, P.D. (2002) U-Pb zircon geochronology, geochemistry and Nd isotopic study of Neoprozoic bimodal volcanic rocks in the Kangdian Rift of south China: Implications for the initial rifting of Rodinia. Precambrian Research, 113, 135–154.
Li, J.W., Zhao, X.F., Zhou, M.F., Vasconcelos, P., Ma, C.Q., Deng, X.D., de Souza, Z.S., Zhao, Y.X., and Wu, G. (2008) Origin of the Tongshankou porphyry-skarn Cu–Mo deposit, eastern Yangtze craton, Eastern China: eochronological, geochemical, and Sr–Nd–Hf isotopic constraints. Mineralium Deposita, 43, 315–336.
Li, J.W., Zhao, X.F., Zhou, M.F., Ma, C.Q., de Souza, Z.S., and Vasconcelos, P. (2009) Late Mesozoic magmatism from the Daye region, eastern China: U–Pb ages, petrogenesis, and geodynamic implications. Contributions to Mineralogy and Petrology, 157, 383–409.
Li, J.W., Vasconcelos, P.M., Zhou, M.F., Deng, X.D., Cohen, B., Bi, S.J., Zhao, X.F., and Selby, D. (2014) Longevity of magmatic-hydrothermal systems in the Daye Cu-Fe-Au district, eastern China with implications for mineral exploration. Ore Geology Reviews, 57, 375–392.
Li, Y., Selby, D., Condon, D., and Tapster, S. (2017) Cyclic magmatic-hydrothermal evolution in porphyry systems: high-precision U-Pb and Re-Os geochronology constraints on the Tibetan Qulong porphyry Cu-Mo deposit. Economic Geology, 112, 1419–1440.
Liu, J.S., Ma, G., and Shu, G.L. (2005) Discovery of cryptoexplosive breccia type Cu (Au) orebodies in Tonglushan skarn-type Cu-Fe deposit of Hubei Province and ore-searching vista. Mineral Deposits, 24, 527–534. (In Chinese with English abstract.)
Meinert, L.D., Dipple, G.M., and Nicolescu, S. (2005) World skarn deposits. In J.W. Hedenquist, J.F.H. Thompson, R.J. Goldfarb, and J.P. Richards, Eds., Economic Geology 100th Anniversary Volume, 299–336. Society of Economic Geologists, Littleton, Colorado.
Meinert, L.D., Hedenquist, J.W., Satoh, H., and Matsuhisa, Y. (2003) Formation of anhydrous and hydrous skarn in Cu-Au ore deposits by magmatic fluids. Economic Geology, 98, 147–156.
Mercer, C.N., Reed, M.H., and Mercer, C.M. (2015) Time scales of porphyry Cu deposit formation: Insights from titanium diffusion in quartz. Economic Geology, 110, 587–602.
Mungall, J.E. (2002) Roasting the mantle: Slab melting and the genesis of major Au and Au-rich Cu deposits. Geology, 30, 915–918.
Nadeau, O., Williams-Jones, A.E., and Stix, J. (2010) Sulphide magma as a source of metals in arc-related magmatic hydrothermal ore fluids. Nature Geoscience, 3, 501–505.
Nadeau, O., Stix, J., and Williams-Jones, A.E. (2013) The behavior of Cu, Zn and Pb during magmatic–hydrothermal activity at Merapi volcano, Indonesia. Chemical Geology, 342, 167–179.
O'Neill, H.St.C., and Pownceby, M.I. (1993) Thermodynamic data from redox reactions at high temperatures. I. An experimental and theoretical assessment of the electrochemical method using stabilized zirconia electrolytes, with revised values for the Fe-"FeO", Co-CoO, Ni-NiO and Cu-Cu_2O oxygen buffers, and new data for the W-WO_2 buffer. Contributions to Mineralogy and Petrology, 114, 296–314.
Park, J.-W., Campbell, I.H., Kim, J., and Moon, J.-W. (2015) The role of late sulfide saturation in the formation of a Cu- and Au-rich magma: Insights from the platinum-group geochemistry of Niuatahi-Motutahi lavas, Tonga rear arc. Journal of Petrology, 56, 59–81.
Park, J.-W., Campbell, I.H., Malaviarachchi, S.P.K., Cocker, H., Hao, H., and Kay, S.M. (2019) Chalcophile element fertility and the formation of porphyry Cu ± Au deposits. Mineralium Deposita, 54, 657–670.
Paterson, B.A., and Stephens, W.E. (1992) Kinetically induced compositional zoning in titanite: implications for accessory-phase/melt partitioning of trace elements. Contributions to Mineralogy and Petrology, 109, 373–385.
Piccoli, P.M., Candela, P.A., and Rivers, M.L. (2000) Interpreting magmatic processes from accessory phases: Titanite—a small-scale recorder of large-scale processes. Transactions of the Royal Society of Edinburgh-Earth Sciences, 91, 257–267.
Pirajno, F., and Zhou, T. (2015) Intracontinental porphyry and porphyry-skarn mineral systems in eastern China: scrutiny of a special case "made-in-China". Economic Geology, 110, 603–629.
Putirka, K. (2016) Amphibole thermometers and barometers for igneous systems and some implications for eruption mechanisms of felsic magmas at arc volcanoes. American Mineralogist, 101, 841–858.
Richards, J.P. (2003) Tectono-magmatic precursors for porphyry Cu-(Mo-Au) deposit formation. Economic Geology, 98, 1515–1533.
——— (2013) Giant ore deposits formed by optimal alignments and combinations of geological processes. Nature Geoscience, 6, 911–916.
——— (2015) The oxidation state, and sulfur and Cu contents of arc magmas: implications for metallogeny. Lithos, 233, 27–45.
Ridolfi, F., Renzulli, A., and Puerini, M. (2010) Stability and chemical equilibrium of amphibole in calc-alkaline magmas: An overview, new thermobarometric formulations and application to subduction-related volcanoes. Contributions to Mineralogy and Petrology, 160, 45–66.
Seedorff, E., Dilles, J.H., Proffett, J.M., Einaudi, M.T., Zurcher, L., Stavast, W.J.A., Johnson, D.A., and Barton, M.D. (2005) Porphyry deposits: Characteristics and origin of hypogene features. In J.W. Hedenquist, J.F.H. Thompson, R.J. Goldfarb, and J.P. Richards, Eds., Economic Geology 100th Anniversary Volume, 251–298. Society of Economic Geologists, Littleton, Colorado.
Seo, J.H., Guillong, M., and Heinrich, C.A. (2009) The role of sulfur in the formation of magmatic–hydrothermal copper–gold deposits. Earth and Planetary Science Letters, 282, 323–328.
Shu, Q.A., Chen, P.R., and Chen, J.R. (1992) Geology of Fe–Cu ore deposits in Eastern Hubei Province, 1st ed. Press of Metallurgical Industry.
Sillitoe, R.H. (2010) Porphyry copper systems. Economic Geology, 105, 3–41.
——— (2012) Copper provinces. In J.W. Hedenquist, M. Harris, and F. Camus, Ed., Geology and Genesis of Major Copper Deposits and Districts of the world: A Tribute to Richard H. Sillitoe. Society of Economic Geologists, Special Publication 16, 1–18.
——— (2018) Why no porphyry copper deposits in Japan and South Korea? Resource Geology, 68, 107–125.
Simmons, S.F., White, N.C., and John, D.A. (2005) Geological characteristics of epithermal precious and base metal deposits. In J.W. Hedenquist, J.F.H. Thompson, R.J. Goldfarb, and J.P. Richards, Eds., Economic Geology 100th Anniversary Volume, 485–522. Society of Economic Geologists, Littleton, Colorado.
Simon, A.C., Pettke, T., Candela, P.A., Piccoli, P.M., and Heinrich, C.A. (2004) Magnetite solubility and iron transport in magmatic-hydrothermal environments. Geochimica et Cosmochimica Acta, 68, 4905–4914.
Song, S., Mao, J., Xie, G., Chen, L., Santosh, M., Chen, G., Rao, J., and Ouyang, Y. (2019) In situ LA-ICP-MS U–Pb geochronology and trace element analysis of hydrothermal titanite from the giant Zhuxi W (Cu) skarn deposit, South China. Mineralium Deposita, 54, 569–590.
Spooner, E.T.C. (1993) Magmatic sulphide/volatile interaction as a mechanism for producing chalcophile element enriched, Archean Au-quartz, epithermal Au-Ag and Au skarn hydrothermal ore fluids. Ore Geology Reviews, 7, 359–379.
Stavast, W.J.A., Keith, J.D., Christiansen, E.H., Dorais, M.J., and Tingey, D. (2006) The fate of magmatic sulfides during intrusion or eruption, Bingham and Tintic districts, Utah. Economic Geology, 101, 329–345.
Tattitch, B., and Blundy, J.D. (2017) Cu-Mo partitioning between felsic melts and saline-aqueous fluids as a function of X_{NaCleq}, f_{O_2}, and f_{S_2}. American Mineralogist, 102, 1987–2006.
Tattitch, B., Chelle-Michou, C., Blundy, J., and Loucks, R.R. (2021) Chemical feedbacks during magma degassing control chlorine partitioning and metal extraction in volcanic arcs. Nature Communications, 12, 1774.
Wang, Q., Zhao, Z.H., Bao, Z.W., Xu, J.F., Liu, W., Li, C.F., Bai, Z.H., and Xiong, X.L. (2004) Geochemistry and petrogenesis of the Tongshankou and Yinzu adakitic intrusive rocks and the associated porphyry copper-molybdenum mineralization in southeast Hubei, east China. Resource Geology, 54, 137–152.
Wang, Q., Xu, J.F., Jian, P., Bao, Z.W., Zhao, Z.H., Li, C.F., Xiong, X.L., and Ma, J.L. (2006) Petrogenesis of adakitic porphyries in an extensional tectonic set-

ting, Dexing, South China: implications for the genesis of porphyry copper mineralization. Journal of Petrology, 47, 119–144.
Wang, R., Richards, J.P., Hou, Z., Yang, Z., and DuFrane, S.A. (2014) Increased magmatic water content—the key to Oligo-Miocene porphyry Cu-Mo±Au formation in the eastern Gangdese belt. Economic Geology, 109, 1315–1339.
Watson, E.B., and Liang, Y. (1995) A simple model for sector zoning in slowly grown crystals; implications for growth rate and lattice diffusion, with emphasis on accessory minerals in crustal rocks. American Mineralogist, 80, 1179–1187.
Wilkinson, J.J. (2013) Triggers for the formation of porphyry ore deposits in magmatic arcs. Nature Geoscience, 6, 917–925.
Williams-Jones, A.E., and Heinrich, C.A. (2005) Vapor transport of metals and the formation of magmatic-hydrothermal ore deposits. In J.W. Hedenquist, J.F.H. Thompson, R.J. Goldfarb, and J.P. Richards, Eds., Economic Geology 100th Anniversary Volume, 1287–1312. Society of Economic Geologists, Littleton, Colorado.
Williamson, B.J., Herrington, R.J., and Morris, A. (2016) Porphyry copper enrichment linked to excess aluminium in plagioclase. Nature Geoscience, 9, 237–241.
Xie, G.Q., Mao, J.W., Li, R.L., Qu, W.J., Pirajno, F., and Du, A.D. (2007) Re–Os molybdenite and Ar–Ar phlogopite dating of Cu–Fe–Au–Mo (W) deposits in southeastern Hubei, China. Mineralogy and Petrology, 90, 249–270.
Xie, G., Mao, J., and Zhao, H. (2011) Zircon U–Pb geochronological and Hf isotopic constraints on petrogenesis of Late Mesozoic intrusions in the southeast Hubei Province, Middle–Lower Yangtze River belt (MLYRB), East China. Lithos, 125, 693–710.
Yang, Z., Lu, Y., Hou, Z., and Chang, Z. (2015) High-Mg diorite from Qulong in southern Tibet: Implications for the genesis of adakite-like intrusions and associated porphyry Cu deposits in collisional orogens. Journal of Petrology, 56, 227–254.
Yu, Y.C., Li, G., Xiao, G.Q., Yang, H.C., Xue, D.K., Liu, Y.L., and Li, J.Z. (1985) The Tonglushan Cu–Fe Skarn Deposit. Geological Team of Southeast Hubei Province, Daye.
Zajacz, Z., and Halter, W.E. (2009) Copper transport by high temperature, sulfur-rich magmatic vapor: Evidence from silicate melt and vapor inclusions in a basaltic andesite from the Villarrica volcano (Chile). Earth and Planetary Science Letters, 282, 115–121.
Zajacz, Z., Halter, W.E., Pettke, T., and Guillong, M. (2008) Determination of fluid/melt partition coefficients by LA-ICPMS analysis of co-existing fluid and silicate melt inclusions: Controls on element partitioning. Geochimica et Cosmochimica Acta, 72, 2169–2197.
Zajacz, Z., Seo, J.H., Candela, P.A., Piccoli, P.M., and Tossell, J.A. (2011) The solubility of copper in high-temperature magmatic vapors: A quest for the significance of various chloride and sulfide complexes. Geochimica et Cosmochimica Acta, 75, 2811–2827.
Zajacz, Z., Candela, P.A., Piccoli, P.M., Wälle, M., and Sanchez-Valle, C. (2012) Gold and copper in volatile saturated mafic to intermediate magmas: Solubilities, partitioning, and implications for ore deposit formation. Geochimica et Cosmochimica Acta, 91, 140–159.
Zhang, D., and Audétat, A. (2017) What caused the formation of the giant bingham canyon porphyry Cu-Mo-Au deposit? Insights from melt inclusions and magmatic sulfides. Economic Geology, 112, 221–244.
——— (2018) Magmatic-hydrothermal evolution of the barren Huangshan Pluton, Anhui Province, China: A melt and fluid inclusion study. Economic Geology, 113, 803–824.
Zhang, L., Ren, Z.Y., Xia, X.P., Yang, Q., Hong, L.B., and Wu, D. (2019) In situ determination of trace elements in melt inclusions using laser ablation inductively coupled plasma sector field mass spectrometry. Rapid Communications in Mass Spectrometry, 33, 361–370.
Zhao, H., Xie, G., Wei, K., and Ke, Y. (2012) Mineral compositions and fluid evolution of the Tonglushan skarn Cu–Fe deposit, SE Hubei, East-Central China. International Geology Review, 54, 737–764.
Zheng, Y.C., Liu, S.A., Wu, C.D., Griffin, W.L., Li, Z.Q., Xu, B., Yang, Z.M., Hou, Z.Q., and O'Reilly, S.Y. (2019) Cu isotopes reveal initial Cu enrichment in sources of giant porphyry deposits in a collisional setting. Geology, 47, 135–138.
Zhou, T., Wang, S., Fan, Y., Yuan, F., Zhang, D., and White, N.C. (2015) A review of the intracontinental porphyry deposits in the Middle-Lower Yangtze River Valley metallogenic belt, Eastern China. Ore Geology Reviews, 65, 433–456.
Zhou, J.-S., Wang, Q., Wyman, D.A., and Zhao, Z.-H. (2020a) Petrologic reconstruction of the Tieshan magma plumbing system: Implications for the genesis of magmatic-hydrothermal ore deposits within originally water-poor magmatic systems. Journal of Petrology, 61.
Zhou, J.-S., Yang, Z.-S., Hou, Z.-Q., and Wang, Q. (2020b) Amphibole-rich cumulate xenoliths in the Zhazhalong intrusive suite, Gangdese arc: Implications for the role of amphibole fractionation during magma evolution. American Mineralogist, 105, 262–275.
Zhou, J.-S., Wang, Q., Xing, C.-M., Ma, L., Hao, L.-L., Li, Q.-W., Wang, Z.-L., and Huang, T.-Y. (2021) Crystal growth of clinopyroxene in mafic alkaline magmas. Earth and Planetary Science Letters, 568, 117005.
Zhu, Q., Xie, G., Mao, J., Li, W., Li, Y., Wang, J., and Zhang, P. (2015) Mineralogical and sulfur isotopic evidence for the incursion of evaporites in the Jinshandian skarn Fe deposit, Edong district, Eastern China. Journal of Asian Earth Sciences, 113, 1253–1267.
Zhu, Q., Xie, G., Mao, J., Hou, K., Sun, J., and Jiang, Z. (2017) Formation of the Jinshandian Fe skarn ore field in the Edong district, Eastern China: Constraints from U–Pb and $^{40}Ar/^{39}Ar$ geochronology. Ore Geology Reviews, 86, 1–20.
Zhu, Q., Xie, G., and Li, W. (2019) Superposition mechanism of Fe enrichment in skarn deposits of Edong district: constrains from magnetite texture and ore grade data. Acta Petrologica Sinica, 35, 3703–3720 (in Chinese with English abstract).

Manuscript received January 3, 2021
Manuscript accepted August 23, 2021
Manuscript handled by Callum Hetherington

Endnote:

[1]Deposit item AM-22-97951, Online Materials. Deposit items are free to all readers and found on the MSA website, via the specific issue's Table of Contents (go to http://www.minsocam.org/MSA/AmMin/TOC/2022/Sep2022_data/Sep2022_data.html).